

# RECRYSTALLIZATION STUDIES IN COMMERCIAL 3004 ALUMINUM ALLOY

*by*

RAJIB BHATTACHARYYA

TH  
me / 1986 / m  
B4698

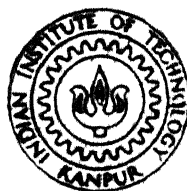
ME

1986

M

BHA

REC



DEPARTMENT OF METALLURGICAL ENGINEERING

INDIAN INSTITUTE OF TECHNOLOGY KANPUR

MAY, 1986

# **RECRYSTALLIZATION STUDIES IN COMMERCIAL 3004 ALUMINUM ALLOY**

*A Thesis Submitted*  
**in Partial Fulfilment of the Requirements  
for the Degree of**

**MASTER OF TECHNOLOGY**

*by*

**RAJIB BHATTACHARYYA**

*to the*

**DEPARTMENT OF METALLURGICAL ENGINEERING  
INDIAN INSTITUTE OF TECHNOLOGY KANPUR  
MAY, 1986**

167 86

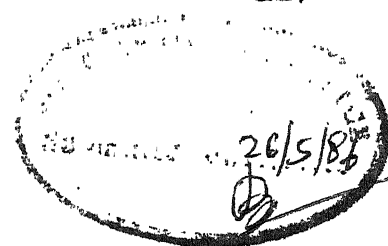
U. T. K. A. S. S. A.  
CENTRAL LIBRARY  
No. A 92061

Th  
669.95722  
B469 Y

ME-1986-M-BHA-REC

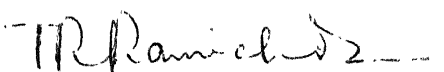
**DEDICATED  
TO  
MY PARENTS**



CERTIFICATE

This is to certify that the thesis entitled,  
'Recrystallization studies in commercial 3004 Aluminum  
Alloy' has been carried out by Mr. Rajib Bhattacharyya  
under my supervision and that the work has not been  
submitted elsewhere for a degree.

May, 1986.

  
(T.R. Ramachandran)  
Professor & Head  
Department of Metallurgical Engg.  
Indian Institute of Technology  
Kanpur-208016

ACKNOWLEDGEMENTS

I am greatly indebted to Prof. T.R. Ramachandran for his efficient guidance and constant cooperation with me during the course of my work at I.I.T. Kanpur. I also express my deep gratitude to Prof. K.P. Gupta and Prof. A.M. Gokhale for their important suggestions in various matters related to my thesis work.

I convey my heartfelt gratitude to all my friends who have helped me in the preparation of the thesis; directly or indirectly. Asim Bag, Sibsankar Haldar, Goutam Bhattacharyya, B. Nandy<sup>and</sup> Nakkalil have helped me in many ways. I am also equally thankful to my friend and project partner Anjan for his constant cooperation and honest advice.

Special note of thanks are due to Dr(s) A. Garg. S. Das, Mr. Sharma and Mr. Jain helped me in all possible ways - I am deeply thankful to them.

Finally but not p<sup>er</sup>functorily, I wish to thank Mr.U.S.Mishra and Mr. R.N.Srivastava for their patience and diligence in typing the thesis.

	<u>CONTENTS</u>	<u>Page</u>
CHAPTER 1	INTRODUCTION	1
1.1	Aluminium-Manganese Alloys	1
1.1.1	Aluminium-Manganese Equilibrium System	2
1.1.2	Al-Fe-Mg-Mn-Si System	4
1.2	Non-equilibrium Structure	5
1.2.1	Aluminum-Manganese System	5
1.3	Effect of Manganese on Properties	7
1.3.1	Physical Properties	7
1.3.2	Mechanical Properties	9
1.3.3	Corrosion Resistance	11
1.4	Commercial Al-Mn Alloys	13
1.5	Purpose of Present Investigation	13
CHAPTER 2	LITERATURE REVIEW	14
2.1	Deformed Structure	14
2.1.1	Pure Metals	14
2.1.2	The Effect of Small Particles	19
2.1.3	The Effect of Large Particles	20
2.2	Recovery	22
2.2.1	Pure Metals	22
2.2.2	Effect of Particle Size	25
2.3	Recrystallization in Al-Mn Alloys	27
2.4	Formation and Growth of Recrystallization Nuclei Around Particle	31
2.5	Criteria for Nucleation	35
2.6	Preferred Orientation	36
2.6.1	Rolling Textures in Aluminum	37
2.6.2	Recrystallization Texture	37
2.6.3	Rolling Recrystallization Textures in Aluminum	38
2.7	Texture Formation in Aluminum Alloys	39
CHAPTER 3	EXPERIMENTAL PROCEDURE	41
3.1	Materials Studied	41
3.2	Nature of Investigations	41
3.3	Processing of Materials	42
3.3.1	Preliminary Treatments	42
3.3.2	Specimens for Different Studies	43
3.4	Electron Microscopy	44
3.4.1	Sample Preparation	44
3.4.2	Information from Electron Micrographs and SADPs	44
3.5	Texture Analysis	45

CHAPTER	4	RESULTS AND DISCUSSIONS	47
	4.1	Introduction	47
	4.2	Texture Studies	47
		4.2.1 Solution-treated Samples	47
		4.2.2 Precipitation-treated Samples	49
	4.3	Electron Microscopic Studies	60
		4.3.1 Nature of Primary Insolubles	60
		4.3.2 Microstructural Studies	60
		4.3.2.1 As-received Samples	65
		4.3.2.2 Solution-treated samples	66
		4.3.2.3 Precipitation-treated samples	72
	4.4	General Discussion	84
CHAPTER	5	CONCLUSION	89
REFERENCES			91
APPENDIX	I	Interplanar Spacings (d) of $\text{Al}_{12}(\text{FeMn})_3\text{Si}$	94
	II	(111) Standard Projection of Cubic Crystals	95
	III	(111) Pole Figure showing (110) $[\bar{1}12]$ Orientations.	96

### ABSTRACT

In the present investigation, the recrystallization behaviour of commercial 3004 Al alloy has been studied by transmission electron microscopy and texture analysis, in solution-treated and precipitation-treated samples under both deformed as well as annealed conditions. The alloy has been deformed to 90% and 60% followed by annealing at 250°C, 300°C and 350°C. Moreover, deformed and annealed (250°C) structures of as-received alloy have also been examined by electron microscopy. Primary insoluble particles remain present in S.T. specimens. They have been found to facilitate recrystallization process in general. The nature of these insolubles have been found to be  $\text{Al}_{12}(\text{Fe}, \text{Mn})_3\text{Si}$  by electron diffraction pattern analysis.

The deformed alloy shows a texture close to (111) [uvw] type, whereas almost all the annealed samples show a rolling texture component along with preference for (023)  $[\bar{3}3\bar{2}]$ , (225)  $[\bar{5}5\bar{4}]$  and (211)  $[\bar{1}1\bar{3}]$  orientations.

## CHAPTER 1

### INTRODUCTION

#### 1.1 Aluminium-Manganese Alloys

The solid-solubility of most alloying elements in aluminium is very limited (1). Its because of the fact that the solubility of a metal with higher valence in a solvent of lower valence is more extensive than for the reverse situation; aluminium is a tri-valent metal whereas most of the alloying elements are di-valent e.g., Mn, Mg, Zn, Cu, Fe to name only a few. Whereas in steels and copper-base alloys, small additions of most alloying elements dissolve in the iron or copper lattice and do not affect the basic structure appreciably, even small additions of most alloying element to aluminum results in the formation of one or more new phases. Thus, whereas most Cu-base alloys or complex steels can usually be handled with binary or ternary diagrams, sometimes with small modification to account for the effect of alloying elements, commercially pure aluminium containing appreciable amounts of Fe and Si is already a ternary alloy (2). Hence, in order to get a reasonably clear picture of the structure of most commercial alloys, complex phase diagrams should be taken into consideration.

Two types of commercial Mn-bearing alloys can be distinguished: the alloys in which manganese is the main

alloying element and those in which manganese plays a subsidiary role and other elements are dominant. In the first group are comprised the Al-Mn and Al-Mn-Mg alloys, whose structures are covered by Al-Fe-Mn-Si and Al-Fe-Mg-Mn-Si systems, respectively. Among the other alloys the most important are the Cu-bearing ones, covered by Al-Cu-Fe-Mn-Si and Al-Cu-Fe-Mg-Mn-Si; and the Al-Zn-Mg alloys covered by the Al-Fe-Mg-Mn-Si-Zn and Al-Cu-Fe-Mg-Mn-Si-Zn systems.

1.1.1 Aluminium-Manganese Equilibrium Diagram: Manganese dissolves in aluminium upto a maximum of 1.8% Mn at eutectic temperature, the solubility decreasing with decreasing temperature (Fig.1). Thus in cooling the Mn precipitates out of solution and there is the possibility of changing the properties through age-hardening treatments, but the change of properties that can be obtained is too small to justify the cost of heat treatment.

The phase in equilibrium with the matrix is  $\text{MnAl}_6$  (25.34% Mn), orthorhombic; lattice parameters,  $a = 6.500 \text{ \AA}$ ,  $b = 7.654 \text{ \AA}$ ,  $c = 8.883 \text{ \AA}$  (3), density  $3250 \text{ kg/m}^3$ , Vickers hardness  $5400\text{--}6500 \text{ MN/m}^2$ . This phase forms an eutectic with aluminium at approximately 1.9% Mn,  $657^\circ\text{C}$ . The  $\text{MnAl}_6$  phase has a limited range of primary crystallization, it forms above 4.1% Mn by peritectic reaction from  $\text{MnAl}_4$ . The typical crystal habit of primary  $\text{MnAl}_6$  is diamond-shaped; most

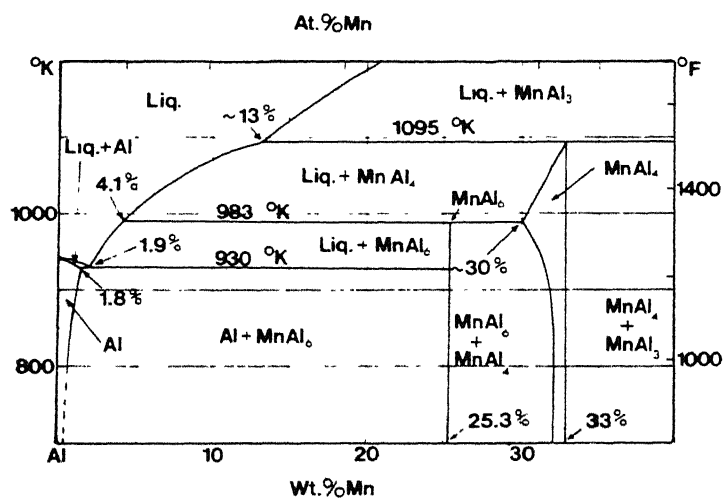


Fig. 1.1 : The aluminium end of the aluminium-manganese equilibrium diagram



often incomplete or hollow, the eutectic habit is often divorced, with  $\text{MnAl}_6$  leading the crystallization and forming sharp cornered crystals and needles resembling primary crystals.

$\text{MnAl}_4$  (33.7% Mn), usually reported as hexagonal, has been recently given the orthorhombic structure with lattice parameters,  $a = 6.795 \text{ \AA}$ ,  $b = 9.343 \text{ \AA}$ ,  $c = 13.897 \text{ \AA}$  (3), density  $3650 \text{ kg/m}^3$ . In alloys containing higher Mn, several other phases are formed but they are of little or no importance for Al-alloys.

1.1.2 Al-Fe-Mg-Mn-Si System: This system is very important commercially because it gives complete coverage of many commercial alloys. Four main groups of alloys are covered: (1) the Mn-bearing, casting alloys with high Si (5-25%), which fall within the 4xxx group, (2) the high-Mg (2-12% Mg) alloys in which Si is usually only an impurity, which fall within the 5xxx group, (3) the alloys in which Mn is the main alloying element and <sup>Mg</sup>  is a lesser addition (3xxx group) and (4) the Mn-bearing alloys with a balanced amount of Mg and Si (6xxx group).

The solidification sequence in the alloys is not completely known; in most commercial alloys aluminium is the primary phase, but there are two exceptions: in some of the high Si ( $\text{Si} > 12\%$ ), Si itself is the primary phase and in some alloys in which manganese is the main addition,

$\text{MnAl}_6$  or  $(\text{FeMn})\text{Al}_6$  is primary. The formula (4)  $\% \text{Mn} = 2 - 1.1\% \text{Fe} - 0.186\% \text{Mg} + 0.32\% \text{Si}$  can be used to calculate the approximate  $\% \text{Mn}$  above which  $(\text{FeMn})\text{Al}_6$  becomes primary in alloys with  $\text{Mg} > \text{Si}$ .

## 1.2 Non-equilibrium Structure

Non-equilibrium structures can be produced either by rapid cooling that suppresses invariant reactions or changes the nucleation of some equilibrium phases; or by heat-treating to high temperature and quenching to retain the high temperature structure. In most aluminium alloys, complete retention of the high temperature structure is not possible and the movement toward equilibrium that takes place may produce new non-equilibrium phases and substantial changes of properties.

1.2.1 Al-Mn System: Fast cooling has an appreciable effect on this system (5). The solid-solubility of manganese in aluminium is increased, and the eutectic point is shifted toward higher Mn-contents. Also fast cooling tends to change the structure of the eutectic from divorced to coupled and consequently the  $\text{MnAl}_6$  crystals change from coarse, angular shapes to a fine, rounded dispersion. When the cooling rate is slow ( $0.01^\circ\text{C}/\text{s}$ ), the manganese in the liquid, diffuses to the growing crystals, so that little or no eutectic is visible. The main effect of rapid cooling

is to increase the undercooling at which nucleation and solidification take place (6). With cooling rates of the order of  $1^{\circ}\text{C}/\text{S}$ , the undercooling is of the order of  $5\text{--}10^{\circ}\text{C}$ . Since the change of structure is a function of the third or fourth power of the undercooling it is obvious that even a few degrees increase in the undercooling for nucleation can have substantial effects. With the extremely fast cooling rates obtainable by splat cooling (rates up to  $10^8\text{--}10^9^{\circ}\text{C}/\text{S}$ ) the undercooling may reach several hundred degrees centigrade (7) and solutions containing up to 15% Mn have been produced.

Another effect of rapid cooling, that is found in alloys containing more than 4% Mn cooled at rates above  $10^3\text{--}10^4^{\circ}\text{C}/\text{S}$ , is the suppression of the peritectic reaction:  $\text{L} + \text{MnAl}_4 \rightarrow \text{MnAl}_6 + \text{Al}$ . Thus in these alloys  $\text{MnAl}_4$  is found, often with a sheath of  $\text{MnAl}_6$ . In more rapidly cooled alloys, nucleation of  $\text{MnAl}_4$  tends to be suppressed, and solid solutions result.

Non-equilibrium structures can also be produced by heat treatment. For most aluminum-alloys heat treatment consists of heating to high temperature to dissolve as much alloying elements, as possible, and then quenching to retain the solid solution. Precipitation follows, and by controlling the stage at which the precipitation is stopped, control of properties can be achieved. The GP zones that form in Al-Mn alloys do not grow far, maximum sizes are of the order of  $10\text{--}15 \text{ \AA}$  thick,  $100\text{--}200 \text{ \AA}$  diameter.

Even in heavily supersaturated alloys the zone formation is slow, little or no transformation take place below 300°C (8) and the nose of the C-curve for the zones is at 500-600°C (9). In this respect the Al-Mn system differs from the normal age hardening Al-alloys, in which zone formation at room temperature is substantial and the nose of the 'C' curves for zone formation is well below 200°C.

Several intermediate phases have been reported for the Al-Mn alloys, some probably due to impurities (10). The only one that is definitely established has the composition of  $\text{MnAl}_{12}$  (14.5% Mn) and is b.c.c.,  $a = 7.48-7.58 \text{ \AA}$  (11)

### 1.3 Effect of Mn on Properties

1.3.1 Physical Properties: The limited information available indicates that boiling point, specific heat, heats of fusion and vaporization and the corresponding entropies etc. are not detectably changed by the amounts of manganese normally added to commercial alloys. This is true also of complex alloys, the above properties are not appreciably different from those of pure aluminium, unless other alloying elements affect them.

The lattice parameters of aluminium solid solution decreases with increasing % Mn. Only the manganese in solid-solution affects the lattice parameter of aluminium solid solution.

Under normal conditions most alloying elements reduce the solubility of manganese in aluminium and hence its effect on the lattice parameter of aluminium. Thus, for example, in the duralumins (which are alloys with 4-5% Cu, 0.5-1.5% Mg, approximately 0.6% Mn, 0.2-0.9% Si, 0.5% Fe) the lattice parameter is strictly dependent on the amount <sup>of</sup> Cu and Mg in solution and the effect of manganese is well within the error of measurement. Only in splat cooled alloys, the effect of manganese can be detected in the multi-component alloys, especially when the other additions have the same <sup>e</sup> effect as manganese.

The density of Al-Mn alloys increases with increasing manganese content. This effect carries on in complex alloys, whose density can be calculated with sufficient accuracy for most purposes by simply summing the effect of various additions.

The increase of electrical resistivity in equilibrium conditions with upto 1.8% Mn in solid-solution is almost linear. At higher Mn content the increase of resistivity is due to the increasing amount of the  $MnAl_6$  phase present. Resistivity in the molten state on the other hand is not appreciably affected by manganese.

Manganese is a common addition to aluminium that (most strongly) raises the magnetic susceptibility. For most elements the effect on the thermal expansion coefficient of

aluminium is roughly inversely proportional to their melting point (12).

1.3.2 Mechanical Properties: Manganese additions to aluminium increase the strength and hardness, and reduce the ductility. Manganese in solution is most effective in increasing the strength, manganese present as undissolved intermetallic compounds has less effect in increasing strength, but more in decreasing ductility. As a consequence of this dependence on dissolved manganese, the mechanical properties are strongly affected by freezing rate: the faster the rate, the more manganese in solution, the higher the strength (Table I).

In most materials an increase of strength, whatever the cause, is associated with a decrease of ductility. However, there is one effect of the manganese that counterbalances this hardening, so that sometimes the decrease of ductility that accompanies an increase of strength is negligible and occasionally an increase of ductility results from the addition of manganese. This effect, that appears especially in high Fe, high Si alloys, results from a change of structure. Many iron bearing compounds crystallize as needles or plates, which are larger, the higher the iron-content. These crystals are usually brittle, and reduce substantially the ductility of the alloys. On the other hand, Mn-bearing compounds, even if some manganese in

them is replaced by Fe, tend to be rounded and do not embrittle the alloys. Thus the manganese addition produces an increase of strength, which is also accompanied by an increase of ductility due to the transformation of shape of the embrittling constituents.

A structural feature of Mn-bearing alloys, that has no important effect on properties, is the "light phenomenon" (13). In casting, manganese tends to segregate into the liquid last to solidify, which collects at the grain boundaries and interdendritic spaces. Homogenization and subsequent working may not be sufficient to diffuse the segregated manganese and Mn-rich zones persist, that are more resistant to etching and give rise to the light striations.

Fatigue resistance depends greatly on the location and distribution of the manganese. With the manganese in solid solution the resistance increases appreciably; a lesser increase results if the manganese is present as well distributed, small, rounded compound crystals. However, if the compound is present as large, sharp-cornered particles, there is an appreciable decrease. This is especially true of the harder alloys, which are more sensitive to the notch effect of sharp-cornered particles.

Strength at high temperature is increased by Mn. Up to 2%, Mn has the highest per unit strengthening effect.

However above 2%, Mn tends to form large primary crystals and its beneficial effect is greatly reduced. Manganese has also some effect on the high temperature strength of cold worked materials. By raising the recrystallization temperature, it permits to retain the cold-worked properties for longer times of high temperature exposure.

TABLE 1 : Mechanical Properties of Al and Al-Mn Alloys

Alloy	Freezing rate (°C/S)	UTS (MN/m <sup>2</sup> )	YS (MN/m <sup>2</sup> )	% Elongation	VHN (MN/
Al 99.99%		45	15	60	120
Al 99%		90	35	40	230
Al 99.99%+1% Mn		65	24	40	220
Al + 1.25% Mn (comm.)	< 1	110	41	35	280
Al+1.25% Mn (comm.)	10 <sup>2</sup>	160	70	15	-
Al+1.25% Mn (comm.)	10 <sup>4</sup> -10 <sup>5</sup>	180	160	5	-

1.3.3 Corrosion Resistance: The most important effect of manganese on aluminium and its alloys is on the corrosion resistance. The Mn-compounds ( $\text{MnAl}_6$ ) formed in aluminium have electrolytic potential that differ only a few mV at most



from the potential of high purity aluminium ( $-0.85$  V) (Electrolytic potential of high purity aluminium in  $\text{NaCl-H}_2\text{O}_2$  solution, against a  $0.1$  N Calomel electrode is  $-0.85$  V). Practically, there is no difference if the manganese is in solution in the aluminium or as compounds, thus Al-Mn alloys are not susceptible to intergranular or stress corrosion. This similarity of potential also means that pitting corrosion is limited even when the compound is less electronegative than aluminium, the amount <sup>of</sup> aluminium that corrodes to protect the compound is minimal. Moreover, a small amount of Cu, of the order of  $0.05$ - $0.20\%$ , dissolved in aluminium, is sufficient to bring the potential of aluminium on the positive side of the compounds. Although the presence of Cu tends to increase the rate of attack (14) when the potential of the matrix is positive to that of the compound, only the compound corrodes and the pit is small and more shallow.

Manganese is reported as a valuable addition to reduce corrosion by mercury. When aluminium comes in contact with mercury, it dissolves into it and an amalgam is formed. The aluminium finely dispersed in the amalgam readily reacts with water vapour in the atmosphere and transforms to hydroxide. More aluminium dissolves into the mercury and the process continues until either the aluminium or the water vapor is exhausted. Manganese dissolved in aluminium hinders the wetting of aluminium by mercury and thus reduces corrosion (15).

#### 1.4 Commercial Al-Mn Alloys

Commercial Al-Mn alloys are vastly used for making cookware, television antenna, car hoods etc. because of their good strength, good corrosion resistance, good formability etc. Chemical compositions of some of the commercial Al-Mn alloys are given in Table 2.

Table 2 : Chemical Compositions of Some Commercial Al-Mn Alloy

Al-Mn alloy	% Mn	% Si	% Fe	% Cu	% Zn	Others	% M
3003	1.0-1.50	0.6 max.	0.7 max.	0.05-0.20	0.10 max.	0.15 max.	-
3004	1.0-1.5	0.3 max.	0.7 max.	0.25 max.	0.25 max.	0.15 max.	0.8-
3105 *	0.3-0.8	0.6 max.	0.7 max.	0.3 max.	0.4 max.	0.15 max.	0.2-

\* 3105 contain about 0.2% max. Cr and 0.10% max. Ti

1.5 Purpose of the Present Investigation: In the present investigation, recrystallization behaviour of XXXX-commercial 3004 Al-alloy, has been studied. The alloy has been cold-worked to various extent followed by thermal treatments at 250°C, 300°C and 350°C. The texture developed has been studied by X-ray diffraction and the microstructures, after various treatments, have been studied by transmission electron microscopy. The nature of the insolubles present has been established by selected area

## CHAPTER 2

### LITERATURE REVIEW

#### 2.1 Deformed Structure

2.1.1 Pure Metals: The grain of a crystal are broken up into small units on being deformed. These units have been observed by Heidenreich (16) for the first time, These are referred to as cells. Very low amounts of deformation (less than 5% for most metals) produce random slip-line traces on thin-foil electron micrographs but as the deformation is increased a greater number of dislocations is produced and a definite cell structure forms. The average cell diameter is usually of the order of 1 to 3 microns. The main features of the cell structure in fcc metals are as follows:

- (a) The cell size is independent of the initial grain-size and decreases to a limiting value after a certain strain.
- (b) Softer metals have higher limiting values of cell size.
- (c) Harder metals have wider cell walls.

The cell interiors are relatively free from dislocation, whereas the walls are regions of high dislocation density. Although many of the cell walls are arranged irregularly, there

is a general tendency for them to be parallel to low index planes, in fcc metals, often in the form of complex twist boundaries. Alignment along the  $\{100\}$ ,  $\{110\}$  and  $\{111\}$  planes is common in Cu, Al and Ni. The dislocation arrangements within the cell walls are complex and are often associated with small loops. The observation that a small cell size appear to be associated with more ragged cell walls appears to be a general rule in both pure metals and alloys. Weissman et al. (17) noted that the misorientation across the cell walls, in Al, was small when the cell structure was first formed, but that as the deformation increased the cell walls became more delineated, and presumably the misorientation increased.

The sharpness of the cell walls formed during plastic deformation varies from metal to metal in a manner which correlates with the stacking fault energy. A stacking fault is bounded by partial dislocations, the width of the fault being inversely proportional to the stacking-fault energy. Metals having a low stacking fault energy (e.g. Cu) produce wide stacking faults during deformation, with the result that cross-slip is hindered and slip distances are consequently short.

It has been inferred (18) that a cell structure results from the ability of screw dislocations to cross-slip out of their original slip-planes and to arrange themselves

in very localized regions which form the walls on relatively strain-free cells. Such an effect will clearly occur in a comparatively easy manner in metals of high stacking fault energy (e.g. Al, Ni, Fe etc.) in which a clearly defined cell structure is usually found.

Gay et al. (19) first reported that solid-solution elements reduced cell-size in deformed metals. The general conclusion in this regard is that increasing the solute content leads to a decrease in stacking fault energy which in turn influences cell size. The behaviour of solid-solution alloys based on solvents having an inherently high stacking fault energy is less clearly understood. In the case of Al-alloy, this arises because of the low solubility of most elements at room temperature and the need for quenching from an elevated temperature in order to retain a range of solid solution composition. Such quenching treatment introduces large numbers of defects (e.g. vacancies) into the structure with the consequent formation of dislocation loops which interfere with the normal processes of cell formation (20). In particular Vandervoort and Washburn (21) found that the strain required to form a cell structure in a quenched material is greater than for a slowly cooled one, since the moving dislocation interact with vacancies to produce jogs which decrease their mobility and their slip distance. Swann (22) has shown that for Al-4% Cu specimen,

cell structure was formed, even after 50% deformation, despite the fact that the dislocation density was much larger than that found in pure Al deformed to a similar extent. Instead the resultant structure was one of bands of high-dislocation density arranged along (111) traces. Similarly, an Al-3% Mg alloy produced a very poorly defined cell structure after 10% deformation.

There is a considerable volume of experimental data which indicate that the level of stored energy in a cold worked material varies not only with the total strain involved but also as a function of individual grain orientation with respect to the applied stress system. Taoka et al (23) using differential calorimetry, demonstrated that the total stored energy resulting from cold-rolling of Fe-5.6 at% Si single crystals was three times larger in crystals of  $\{110\} \langle 001 \rangle$  orientation than in crystals of  $\{100\} \langle 001 \rangle$  orientation. Every et al. (23) obtained a similar result, but made the further observation that the cell shape was also a function of the grain orientation, being elongated for  $\{110\}$  (high energy) and equiaxed for  $\{100\}$  (low energy) orientations. Dillamore et al. (36) investigating 70% cold-rolled Al-killed steel and pure iron, used TEM to demonstrate that there were increasing levels of stored energy in grains in the orientation order  $\{001\} \langle 1\bar{1}0 \rangle$ ,  $\{111\} \langle 1\bar{1}0 \rangle$ ,  $\{110\} \langle 1\bar{1}0 \rangle$ . They also demonstrated that the increased stored energy was associated

with both a smaller cell size and a larger average cell boundary misorientation.

The above data are supplemented by further results which indicate that there can be important variations in the nature and extent of stored energy of cold work within individual grains. The necessarily more complex deformation pattern near grain-boundary regions can produce microstructures which differ from those in regions nearer grain centres. In particular, deformation cell structures in boundary region can be smaller, or more elongated, or have larger mean boundary, misorientation and there may be cumulative misorientations between the boundary and grain centre regions.

Alternatively, large scale differences both in orientation and microstructure may exist within individual grains which are suitably oriented to undergo deformation bending during cold work. Further more, recent work has emphasised that the imposition of large strain can cause grains to be crossed and subdivided by microscopic shear bands of complex and fine scale internal microstructure.

Other investigators (23) have noted that small interface segments of high angle misorientation are generated at intragranular sites during deformation. This type of feature has been observed in Al, Cu and Fe - 0.007 wt.% C wire. Since these boundary segments occur more frequently at

higher deformation levels, it seems likely that they may contribute to the in-situ recrystallization which has been reported in some very heavily cold worked materials.

2.1.2 The Effect of Small Particles: The basic differences which exist between the deformation microstructures in particle free and particle containing materials originate from an interference with free movement of dislocations in particle containing alloys. Extensive studies of different alloy systems, mainly deformed to low total strain, have shown that small particles stimulate both dislocation loop formation (23) and an increased frequency of cross-slip. It is also clear that the presence of distributions of small particles tends to retard the formation of dislocation cell structures. Cell structures which are formed in materials containing distributions of small particles tend to be considerably smaller, at similar deformation levels, than in the corresponding particle free materials.

The magnitude of both random and long range orientation differences in deformed materials containing distribution of small particles is also different <sup>from</sup> / that generated in particle-free material. Evidence of this comes from a study by Brimhall et al. (23) of a rolled Ag-MgO alloy, where a reduction in both random and long range orientation differences was found in comparison to pure Ag.



2.1.3 The Effect of Large Particles: During cold-working a region with high dislocation density is formed around large non deformable particles ( $> 1 \mu\text{m}$ ). This region is referred to as the deformation zone. In Al alloys, a well developed sub-structure is present (24,25). The subgrain size is considerably smaller than in the matrix outside the deformation zone. The misorientation of the subgrain relative to the matrix is large in particular close to the particle.

A model for the deformation zone proposed by Sandstrom (26), predicts that the width ' $\lambda$ ' of the deformation zone measured from the particle surface is proportional to the particle diameter 'd'

$$\lambda = \alpha d \quad (1)$$

where the constant ' $\alpha$ ' is about 0.8 and 1.0 for 50% and 95% cold reduction respectively for Al. This relation is in perfect agreement with the observations of Humphreys (24) and of Herbst and Huber (25). Once the width of the deformation zone which is assumed to be spherically symmetrical is known its dislocation density can be evaluated from the amount of geometrically necessary dislocation in the zone.

Another important parameter is the maximum misorientation,  $\theta_m$  across the deformation zone. With the help of a continuum mechanics model Humphreys (24) proposed the following

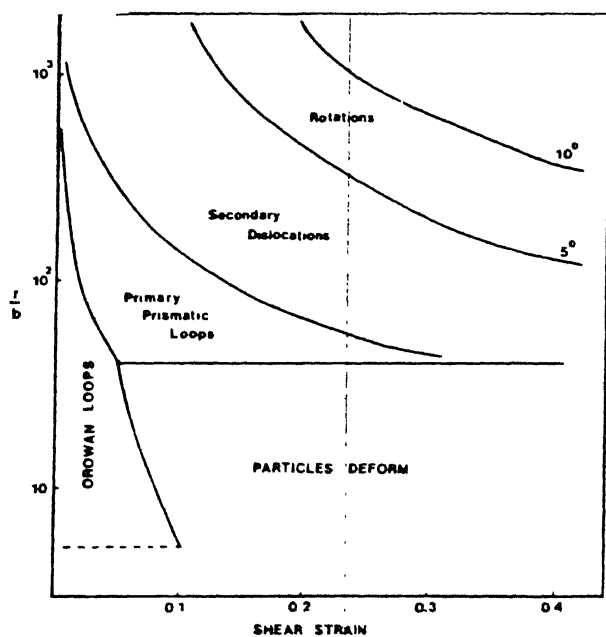


Fig. 2.1 : Deformation mechanisms at particles as a function of shear strain and particle radius ( $r$ ).

relationship:

$$\Theta_m = \epsilon d / 3\lambda \quad (2)$$

where  $\epsilon$  is the true strain of the cold reduction. For small strains  $\sim 0.1$  ( $\lambda \sim 0.5 d$ ),  $\Theta_m$  is about  $0.7\epsilon$ . For large strains  $\epsilon > 2$  ( $\lambda \sim d$ ),  $\Theta_m$  is about  $0.3\epsilon$ . To obtain a maximum misorientation of at least  $10^\circ$  typical for a high angle boundary, the cold reductions must exceed 30%.

For the comparatively simple case of an alloy such as Al-Si containing well separated, strong, equiaxed particles in a single crystal deforming predominantly on one slip system at low temperatures, the dislocation structures produced near particles at which voids do not form are shown in Fig. 2.1 (27). The formation of large local lattice rotations is seen to be favoured by large particles and strain. The subgrains in the deformation zone appear to be equiaxed and of mean size  $\sim 0.1 \mu\text{m}$ . The subgrain size does not vary greatly with strain, or particle size and no systematic variation with position in the deformation zone has been detected. For elongated particles, the misorientation are greatest at the end of the particles.

## 2.2 Recovery

2.2.1 Pure Metals: In many materials the recovery of dislocation substructures starts during the deformation process

itself. This is reflected by the fact that changes in both the size and shape of subgrains with increasing levels of deformation do not completely mirror macroscopic changes in specimen or grain shape or size. Swann (23) showed that subgrain sizes in rolled Al decreased to a limiting value of about  $2\text{ }\mu\text{m}$  after 30% deformation and remained virtually unchanged thereafter.

At lower total strains, or in materials where a cell rather than a clear subgrain structure tends to form during deformation, dislocation recovery appears to occur in two relatively distinct phases on subsequent annealing (23). The first stage involves a sharpening of the cell walls to form clearer subgrain boundaries, accompanied by a reduction in the dislocation density in cell interiors, during which there seems to be no noticeable increase in subgrain size. There is evidence that this local redistribution of dislocations is favoured in region adjacent to grain and twin boundaries. Subsequent changes in microstructure prior to nucleation of recrystallization occur principally as a result of subgrain growth. Dillamore et al. (36) found that growth rates differed from grain to grain, depending on individual grain orientation. For a range of annealing temperatures, in 70% cold-rolled high purity Fe, they found that subgrain structures in  $\{111\} \langle \bar{1}10 \rangle$  and  $\{110\} \langle \bar{1}10 \rangle$  oriented grains coarsened more rapidly than in either  $\{001\} \langle \bar{1}10 \rangle$  or  $\{113\} \langle \bar{1}10 \rangle$  oriented grains. They also found that the subgrain growth rate differences to be

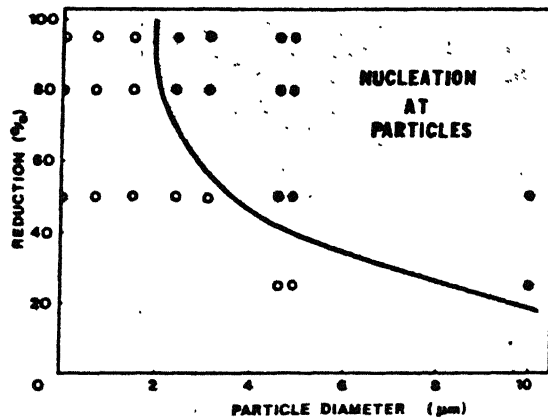


Fig. 2.2 : The conditions of strain and particle size for which recrystallization is nucleated at particles .

considerably larger than could be accounted for in terms of the initial grain specific differences in stored energy level, and, on the basis of a computer model of subgrain growth, suggested that differences in width of the initial subgrain size distributions was an important factor in the subsequent development of differences in subgrain growth rates. Wider initial subgrain size distributions characterised the faster growing subgrain in  $\{111\} \langle \bar{1}10 \rangle$  and  $\{110\} \langle \bar{1}10 \rangle$  orientation. The additional observation that the width of these subgrain size distributions increased with increases in the mean subgrain size is of particular interest, since the development of recrystallization nuclei will be favoured by the formation of large subgrain in regions of smaller mean subgrain size. A further factor in the recovery process, again specifically relevant to subsequent nucleation of recrystallization, was reported by Faivre et al. (37). They in a study of compressed and annealed Al, found that the distribution of subgrain boundary misorientations also increased during annealing.

**2.2.2 Effect of Particle Size:** For alloys containing widely spaced particles, the minimum size of particles at which recrystallization occurs is found to be  $\sim 1 \mu\text{m}$  in a variety of alloy system. The critical particle size increases as the strain is reduced (24) (Fig. 2.2). The number of recrystallization nuclei formed at a particle is also a function of

particle size. For particles in the size range 1-5  $\mu\text{m}$  (24), usually only one grain is nucleated, but at particles larger than  $\sim 10 \mu\text{m}$ , multiple nucleation is frequently observed (25).

However, the presence of high density of dispersoids will inhibit recovery and grain growth due to their pinning of subgrain and grain boundaries. Obviously, the rate of nucleation of recrystallization will be reduced. Nobili et al. (23) in a study of recovery in Al-Al<sub>2</sub>O<sub>3</sub> alloys, noted that the relative amount of stored energy removed during recovery prior to recrystallization, increased with an increase in the volume fraction of the particles present. At the same time, it was suggested that the distribution of the particles was also likely to be a factor in influencing recovery behaviour. This latter point was emphasized by the work of Hansen and Bay (38) who found different recovery microstructures and subsequent recrystallization behaviour in Al-0.6 and 1.2 wt% Al<sub>2</sub>O<sub>3</sub> alloys where identical volume fractions of particles of identical size and shape were distributed either uniformly or in network.

The above noted results of Nobili and DeMaria (23), imply that the stored energy of cold work is continuously reduced as nucleation of recrystallization is delayed to longer times. Thus it can be expected that with increasing delay, the critical size of subgrain necessary to form a viable recrystallization nucleus will also be larger (23). Other factors,

which are independent of recovery time, will also contribute to an increase in the size of a critical nucleus in materials containing distribution of small particles. These include both direct particle pinning, acting on a potential nucleus interface, and the reduced long range change in lattice orientation brought about by the modified pattern of deformation in these materials.

There is also some experimental evidence which indicates that the presence of a distribution of small particles in an alloy can lead to change in preference to the sites at which nucleation of recrystallization occurs. Hansen et al. (38) reported a tendency for nucleation of recrystallization <sup>to</sup> be biased towards grain boundaries in alloys containing distribution of small particles. A retardation in the growth of subgrain structures caused by small particles, is generally assumed to be the result of Zener pinning of migrating low angle boundaries in a manner analogous to the pinning of high angle boundaries during grain growth.

### 2.3 Recrystallization in Al-Mn Alloys

Manganese has a strong influence on the recrystallization behaviour of aluminium, its effect depending on the supersaturation of the alloy and on the size and distribution of the precipitate particles (28). However, the effect of manganese may be negligible when elements such as



chromium and zirconium (those which have a strongly retarding effect on recrystallization) are present. Precipitation from supersaturated solutions of pure Al-Mn alloys is sluggish (29), also manganese atoms show a marked tendency to segregate to the defects in aluminium. Impurities such as iron and silicon present in commercial alloys affect the diffusion of manganese in aluminum and the free energy of the manganese-containing phases with the result that nucleation and growth characteristics of these phases are changed considerably (30). The process of recrystallization can be affected by the segregation of solutes to defects and by precipitation of a new phase. Thus a strong reciprocal action is seen to exist between recrystallization and precipitation processes.

The recrystallization behaviour of Al-Mn alloys has been studied by a number of investigators. Gatto et al (28) have studied the annealing behaviour of deformed Al-1.04% Mn alloy containing all the manganese in solid solution in one case and a dispersion of precipitates particles in the other. The salient observations are: (i) cell structures occur at lower deformation and develop more regularly and homogeneously in the solution-treated specimens than in those containing precipitate particles and (ii) when the amount of deformation is small, recrystallization occurs at higher temperatures in specimens subjected to precipitation anneal; the effect is reversed for large deformation.

The results have been interpreted on the basis of homogeneous distribution of solute atoms in the solid-solution alloy at high temperatures. Segregation effect present at relatively low temperatures might hinder subgrain development and thereby retard the annealing process. In alloys containing a dispersion of precipitate particles, the hindering effect is caused only by the particles and is independent of temperature as long as coarsening is negligible.

Goel et al. (29) have investigated the reciprocal action between precipitation and recrystallization in Al-0.7% Mn and Al-30% Mn alloys. A well defined cell structure with a mean cell size of  $\sim 1.5\mu\text{m}$  has been observed in the dilute alloy after severe deformation. The recrystallization mode has been found to vary with temperature. For temperature less than  $320^{\circ}\text{C}$ , continuous recrystallization resulting in a very fine grain-size has been observed, the whole process being governed by the effects of segregation and precipitation of manganese on the subgrain structure. Discontinuous recrystallization has been observed in the temperature range  $320^{\circ}\text{--}350^{\circ}\text{C}$  with precipitation occurring on the recrystallization front leading to an intermittent motion of the grain boundary. The distribution of the final grain size has been found to be non-homogeneous. Recrystallization has been observed to be independent of precipitation in the temperature range  $350^{\circ}\text{--}390^{\circ}\text{C}$  and the final grain-size

to be relatively uniform. In the time interval during which recrystallization and precipitation occurred simultaneously, no precipitate particles could be observed on the recrystallization front; they could only be seen on the grain-boundaries in the recrystallized area. The process of recrystallization has been found to go to completion before the onset of precipitation at temperatures exceeding  $390^{\circ}\text{C}$ . Some differences have been noticed in the annealing of lightly-deformed Al-0.7% Mn alloy. The original grain-boundaries, incompletely destroyed during deformation have been found to bulge into the neighbouring grains during low temperature annealing. The tendency for bulging decreased with increasing annealing temperature. The various recrystallization modes reported for the severely deformed samples have been found to occur at slightly higher temperatures in the lightly deformed samples. Recrystallization in several deformed Al-3% Mn alloy has been found to be continuous at lower temperatures and discontinuous at higher temperatures. Precipitate particles have been observed on the recrystallization front as well as in the deformed structure. A significant result is the slight acceleration of recrystallization by the particles precipitated on the sub boundaries. It has been suggested that in the progress of decomposition of the supersaturated solid solution, the growing precipitate particles induce the formation of recrystallization fronts on the boundary surfaces with the matrix. Recrystallization

temperature has been found to increase with increase in Mn content upto a certain level; however, increasing instability of the supersaturated solution causes an acceleration of the process.

#### 2.4 Formation and Growth of Recrystallization Nuclei Around Particles

It is well established that a fine particle dispersion inhibits both the grain nucleation and growth rates while coarse particles ( $> 1\mu\text{m}$  dia.) stimulate the nucleation rates by acting as nucleation sites and reduce the recrystallized grain size which is of great technical importance. A three stage model describes the growth of a potential nucleus in terms of (1) formation of a nucleus by subgrain growth; (2) growth in the deformation zone and (3) growth outside the deformation zone. The most critical event for the survival of the nucleus is general the initial growth in the matrix outside the deformation zone (i.e. step III).

Since no high angle grain boundaries are present initially in general they must be formed. This is assumed to occur by subgrain growth. The most probable situation is that a subgrain which is slightly larger than its neighbours grows at the expense of them. According to Sandstrom (31,32) this growth is controlled by the following equation:

$$\frac{dR}{dt} = \frac{11}{2} \alpha_1 M \tau \left( \frac{1}{R_m} - \frac{1}{R} \right) \quad (3)$$

where ' $R_m$ ' and ' $R$ ' are the radius of the largest and the average sized subgrain respectively.  $\alpha_1$  is a constant of about unity,  $M$  the climb mobility of the dislocations, and  $\tau$  the dislocation line tension.

At the same time as the subgrain grows its boundary misorientation increases. This is a consequence of the variation of the lattice orientation from the boundary of the deformation zone to the particle surface. When the boundary misorientation of the potential nucleus becomes sufficiently large, migration by high angle boundary processes becomes important; when they start to dominate, the transition to the next stage is assumed to take place.

continues

A nucleus formed in the deformation/ to grow by high angle processes. The growth can be described by the following equation (31,32)

$$\frac{dR}{dt} = \beta m (\tau \rho_{dz} - \frac{2\gamma}{R}) \quad (4)$$

where ' $R$ ' is the radius of the nucleus,  $\beta$  a constant of about unity,  $m$  the grain boundary mobility,  $\rho_{dz}$  the dislocation density in the deformation zone, and ' $\gamma$ ' the surface energy per unit area of the nucleus. The growth rate initially rises due to the increase of ' $m$ ' with increasing boundary misorientation. Once the high angle plateau has been reached, ' $m$ ' is approximately constant and

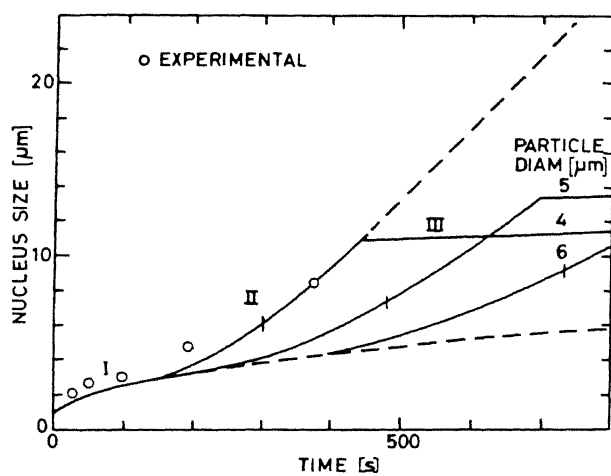


Fig. 2.3 : Diameter of recrystallization nucleus versus time for three different particle diameters 4,5 and 6  $\mu\text{m}$  . . .

consequently also the growth rate. The surface energy term in eqn.(4) is in general small compared to  $\tau\rho_{dz}$  in the deformation zone. The growth continues in this way until the whole deformation zone is consumed. A transition now takes place to the third stage, involving growth outside the deformation zone.

The growth of the nucleus outside the deformation zone is controlled by the same process as in stage II. The growth rate can again be described by the eqn.(4), except that  $\rho_{dz}$  has to be replaced by the dislocation density in the matrix  $\rho_{\text{matrix}}$ . This is less than  $\rho_{dz}$  and hence the surface energy term  $\frac{2\gamma}{R}$  has a correspondingly larger influence on the growth rate.

If the recovery of the dislocations is controlled by the coarsening of the substructure the time dependence of  $\rho_{\text{matrix}}$  can be expressed as  $\rho_{\text{matrix}} \propto \frac{1}{\sqrt{t}}$  (32). In this case parabolic growth  $R \propto t^{1/2}$  is obtained from eqn.(4). The influence of recovery on  $\rho_{dz}$  is small since the density in the deformation zone is mainly made up of geometrically necessary dislocations.

The growth of a nucleus around a nondeformable particle in Al is illustrated in Fig. 2.3. The three stages of growth are easily identified. The subgrain growth in stage I gives a comparatively slow parabolic growth. The growth in stage II is considerably accelerated

due to high angle processes. The vertical bar on the curve gives the position where the high angle plateau for the mobility is reached. Outside the deformation zone in stage III the growth rate is considerably smaller than in stage II due to the lower dislocation density. The influence of the particle diameter is also shown. The particle diameter has initially a rather strong effect on the growth rate but for longer time this difference tends to be washed out. On the other hand the growth rate increases quite rapidly as a function of increasing cold reduction (26).

## 2.5 Criteria for Nucleation

The following criteria for nucleation of recrystallized grains are worthy of consideration:

- (1) The nucleus must obtain high angle boundaries in the deformation zone: In principle the high angle boundaries could be generated by subgrain growth outside the deformation zone. However, since the subgrain are in general randomly oriented in the matrix this would be an extremely slow process and is not of practical importance. For the formation of high angle boundaries within the deformation zone, the maximum misorientation across the zone  $\Theta_m$  must exceed typically about  $10^\circ$ . This implies that the cold reduction must exceed 30%.



(2) The critical size of the nucleus must be smaller

than the total extent of the deformation zone: The most critical stage for the survival of the nucleus is in most cases when the nucleus has consumed the deformation zone and should continue to grow out into the matrix where the dislocation density is lower. From the eqn. (4)

$$\frac{dR}{dt} = \beta_m (\tau \rho_{dz} - \frac{2\gamma}{R}), \text{ it is} \quad (4)$$

evident that for growth to continue  $\frac{dR}{dt}$  must be  $> 0$  ( $\rho_{dz}$  replaced by  $\rho_{\text{matrix}}$ ). This gives the following criterion

$$\lambda + \frac{d}{2} > R_{cr} = \frac{2\gamma}{\tau \rho_{\text{matrix}}} \cdot (31, 32) \quad (5)$$

where  $R_{cr}$  is the critical radius for nucleation.

## 2.6 Preferred Orientation

A polycrystalline material consists of a number of grains; each grain usually has a crystallographic orientation which is different from that of its neighbours. Now, if the grains tend to cluster about some particular orientation or orientations, this condition is said to have a preferred orientation or texture.

In cold-rolled sheet, most of the grains are oriented with a certain plane roughly parallel to the sheet surface, and a certain direction in that plane

roughly parallel to the direction in which the sheet was rolled. These are called deformation textures. Basically, they are due to the tendency for a grain to rotate during plastic deformation.

2.6.1 Rolling Textures in Aluminum: The principal orientation is usually described as one in which a plane of the form  $\{110\}$  is parallel to the rolling plane and a direction of the form  $\langle 112 \rangle$  is parallel to the rolling direction, which may be written  $(110) \parallel \text{rolling plane } [\bar{1}12] \parallel \text{rolling direction}$ , or simply  $(110) \parallel [\bar{1}12]$ . The other possible orientation is  $(112) \langle 11\bar{1} \rangle$ . In addition to the two principal orientations tested, traces of the orientation  $(135) [\bar{5}3\bar{3}]$  have been found. Quantitative pole figures determined by modern-Geiger counter methods have led Hu and Beck (33) to conclude that the texture near the center of rolled Aluminium sheet is best described by an ideal orientation near  $(123) [\bar{1}\bar{2}1]$ . If a sheet is rolled in one direction only, the pole figure is not symmetrical about the transverse direction.

2.6.2 Recrystallization Texture: When a cold-rolled metal or alloy, possessed of a deformation texture, is recrystallized by annealing, the new grain structure usually has a preferred orientation too, often different from that of the cold-worked

material. This is called an annealing texture. Such textures are due to the influence which the texture of the matrix has on the nucleation and/or growth of the new grain in that matrix. The development of recrystallization texture can be explained by two theories (35). In the 'oriented nucleation theory' recrystallization texture formation is solely attributed to a selection of certain orientations in the nucleation process. Once the grains have been nucleated, they are assumed to grow at the same rate, independent of their orientation. The 'oriented growth theory', on the other hand assumes that the orientation of the nuclei is random and the growing grain undergoes a selection process according to their different growth rates due to different crystal orientations.

2.6.3 Rolling Recrystallization Textures in Aluminium: The annealing texture of 99.5% Al sheet was found to be  $(236)[335] + (100)[001] + (110)[\bar{1}\bar{1}0]$  after annealing at 235° to 300°C, with  $(236)[335]$ , and later also  $(110)[\bar{1}\bar{1}0]$  disappearing in favour of  $(100)[001]$  during annealing at 500°C; traces of some of the recrystallization orientations existed in the deformation texture prior to recrystallization.

Beck and Hu (33), using a Geiger counter, found that the maxima in a precision pole figure of 2S aluminum strip annealed at 300°C could be described as a retention of the rolling texture, which is not very far from  $(123)[\bar{1}\bar{2}1]$ ,

plus the cube texture. They point out that a  $[111]$  direction of each of the four symmetrical components of the rolling texture and of the cube texture nearly coincide. Microscope observation showed that polygonization plays a part in retaining the deformation texture, as does also the growth of grains with the orientation of one component into strained material of another component (in an adjacent deformation band) related to the first by a rotation of about  $38^\circ$  around a common axis  $[111]$ .

## 2.7 Texture Formation in Al-alloys

Chan and Humphreys (34) carried out texture studies in an Al-6 wt% Ni alloy deformed to 95% by cold-rolling and then annealed at  $330^\circ\text{C}$ . The rolling texture of the alloy, although weak, was found to be similar to that of deformed single phase Al. Weakening of the texture by the large volume fraction of large second phase particles ( $\approx 1.1\ \mu\text{m}$ ) was ascribed partly to the large volume of the material occupied by the deformation zones at the particles.

The orientation of the recrystallization nuclei was found to be almost random. With the majority of nuclei being misoriented by  $15\text{--}45^\circ$  from the adjacent matrix, and this was interpreted in terms of nucleation within the deformation zone at the particles. In the fully recrystallized ( $503^\circ\text{K}$ , 17h) material, however, the texture was significantly sharper than in the deformed material and this was ascribed to

the more rapid growth of grain of selected orientations. Although particle stimulated nucleation causes a randomization of the texture in the early stages of recrystallization, a fairly sharp final recrystallization texture results. Herbst and Huber (25) also reported random orientation of the recrystallized grain in aluminum alloys.

Bleck and Bunge (35) studied texture behaviour of recrystallized AlMn 1 alloy both in the solution treated (at 600°C for 24 h) as well as precipitation-treated (at 400°C for 5 h subsequent to solution-treatment) alloy. They found the rolling texture to be (112)  $[\bar{1}1\bar{1}]$  (110)  $[\bar{1}12]$  and (123)  $[41\bar{2}]$  for both solution and precipitation treated samples deformed to 95%. After recrystallization at high-temperature the solution treated alloy formed the cube texture and the orientation distribution of the recrystallized grain in the precipitation treated alloy was nearly random with only a slight preference of the rolling texture and cube texture positions. Grain growth after prolonged annealing had been found to enhance slightly the cube orientation with respect to the other orientations.

## CHAPTER 3

### EXPERIMENTAL PROCEDURE

#### 3.1 Materials Studied

In the present investigation a commercial 3004 aluminum alloy has been studied using transmission electron microscopy and X-ray diffraction. The chemical composition of the alloy is given in the Table 3.1.

Table 3.1 : wt%

Alloy	Mn	Mg	Fe	Si	Cu	Ti	Al
3004	1.1	1.29	0.56	0.21	0.001	0.01	bal.

The alloy has been received in the form of 2 cm thick sheets from Indian Aluminium Company, Calcutta.

#### 3.2 Nature of Investigations

The following studies have been conducted on the alloy:

- i) The as-received alloy was solution heat treated at 620°C for 24 h, deformed to various extents by cold-rolling and then annealed at various temperatures. Both deformation and annealing characteristics were studied. These samples will henceforth be

referred to as solution treated (S.T.) samples.

- ii) A precipitation treatment at 400°C subsequent to solution treatment, was given to some samples. These samples will henceforth be referred to as precipitation-treated (P.T.) samples. The precipitation-treated samples were thereafter deformed to various degrees and annealed. Both annealing and deformation behaviour were studied.
- iii) Deformed and annealed characteristics of as-received alloy.
- iv) Grain-orientation studies were done for both solution-treated and precipitation-treated samples in both deformed and annealed states. This experiment was carried out in an ILO-DEBYEFLEX 2002D x-ray diffractometer.

Electron-microscopic studies have been carried out on a Philips EM 301 TEM operated at 100 kV.

### 3.3 Processing of Materials

#### 3.3.1 Preliminary Treatments

Before any measurement or observation is made, each sample has been subjected to the necessary thermal and/or mechanical treatments. All heat treatments have been carried out either in a tubular, horizontal electrically heated airfurnace or in a salt bath. The temperature of

the furnace has been maintained at the required level and controlled to an accuracy of  $\pm 5^{\circ}\text{C}$  by using an Electromax temperature controller. The furnaces were calibrated by using a chromel-alumel thermocouple and Leeds and Northrup millivolt potentiometer. At the end of the heat treatment, all the samples were quenched directly in water. All mechanical treatments have been given by cold rolling to the desired degree of reduction in thickness. All the rolling operations have been carried out between a pair of hardened steel rolls on a two-high rolling mill.

### 3.3.2 Specimens for Different Studies

Small pieces (30 mm x 25 mm x 5 mm) have been cut from the as-received material and rolled down to thicknesses such that subsequent to homogenization treatment at  $620^{\circ}\text{C}$  for 24 h in case of solution-treated samples and homogenization plus precipitation treatment ( $400^{\circ}\text{C}$  for 1, 3 and 12 h) in case of precipitation-treated samples, when all these samples have been rolled down to a final thickness of 0.4 mm, they have been subjected to different degrees of deformation, say 90%, 60% etc. Specimens for texture analysis (25 mm x 15 mm x 0.3 mm) and electron microscopy (20 mm x 15 mm) have been cut out of these strips. These specimens were further annealed at  $250^{\circ}\text{C}$ ,  $300^{\circ}\text{C}$  and  $350^{\circ}\text{C}$  for 1 h, in a salt bath. Deformed and annealed structures



were observed on samples subjected to solution treatment and precipitation treatment.

### 3.4 Electron Microscopy

#### 3.4.1 Sample Preparation

Pieces of  $20 \times 15 \text{ mm}^2$ , cut from the 0.4 mm thick rolled strips have been used for the preparation of thin foils for electron microscopy. After proper thermal treatments the pieces have been chemically thinned down to a thickness of about 0.1 mm using a solution of con.  $\text{H}_3\text{PO}_4$ , conc.  $\text{H}_2\text{SO}_4$ , conc.  $\text{HNO}_3$  in the ratio of 70:20:10 (by volume) heated to  $70^\circ\text{--}80^\circ\text{C}$ . The chemically thinned samples have been subjected to electropolishing for the preparation of thin foils using an electrolyte of ethanol and perchloric acid in the ratio of 80:20 (by volume). Electropolishing has been carried out at around  $0^\circ\text{C}$  which could be obtained by liquid nitrogen or crushed ice. The voltage has been kept between 12–17V and the current density  $0.1\text{--}0.5 \text{ A/cm}^2$ . The standard window technique has been adopted for preparing the thin foils.

#### 3.4.2 Information from Electron Micrographs and Electron

**Diffraction Patterns:** The morphology and size distribution of insoluble and precipitate particles have been obtained from the electron micrographs while the nature of the particles have been established by analysing

the electron diffraction patterns. In order to determine the size of the particles, the following formula was used (39)

$$\overline{D}_s = \frac{3}{2} \pi \frac{A_A}{L_A}$$

where  $\overline{D}_s$  = Average particle size

$A_A$  = Projected area of particle/unit area of micrograph

$L_A$  = Projected perimeter of particle/unit area of micrograph.

However, the above relation is applicable only in case of convex-shaped particles.

The analysis of selected area diffraction patterns was carried out by the ratio method; in this method the ratio of the distances of the elementary diffraction spots gives the inverse ratio of the interplanar spacings, the latter can be compared with standard ratios for the various phases. Confirmation of the exact indices, assigned to the diffraction spots can be obtained from angular measurements.

### 3.5 Texture Analysis

Texture studies were carried out both for solution-treated and precipitation-treated samples in the deformed as well as annealed states. The dimension of each sample

was (25 mm x 15 mm x 0.3 mm). The surface layer of each sample was removed by chemical polishing using the same chemical reagent as that used for the chemical polishing of electron microscopic samples.

The measurements have been carried out using Schulz's reflection method. The diffracted beam intensity is measured by the scintillation counter.

## CHAPTER 4

### RESULTS AND DISCUSSIONS

#### 4.1 Introduction

Electron microscopic and texture studies have been carried out on the cold-worked as well as annealed alloy for both the solution-treated and precipitation-treated samples. Attempt has been made to correlate the results obtained by these studies. The effect of particles on recrystallization and texture behaviour has also been investigated.

#### 4.2 Texture Studies

Texture analysis was carried out by X-ray diffraction. Solution-treated and precipitation-treated samples were studied both in the cold-worked as well as annealed state. A brief account of the results is given below.

4.2.1 Solution treated Samples: Study of (111) pole-figures for cold-worked samples [Figs.4.1(a), 4.2(a), and 4.3 ], deformed to 90%, 60% and 40%, clearly show that the rolling plane is almost parallel to (111) plane for various degrees of deformation. However, it is not possible to find out the rolling-direction from a study of one quadrant only, hence the rolling texture for the worked

alloys is almost  $(111) [\bar{u}vw]$  type. Moreover, the cold-worked 60% sample has a texture component close to  $(\bar{1}23) [210]$  type along with a  $(111) [\bar{u}vw]$  type component [Fig. 4.2(a)]. The texture components were found out by rotation on a Wulff net about relevant axes.

It has been found that the texture developed is very weak in general; this is possibly due to the presence of primary insoluble particles ( $\sim 1.1 \mu\text{m}$ ) in the S.T. samples. This is so probably because of the fact that the deformation zone at the large particles occupy large volume of the material, thereby lowering the tendency for texture formation (34). The annealed samples, in general show that the rolling-texture component is present even after annealing [Figs. 4.1(b), 4.1(c) and 4.2 (b) ]. Figure 4.1(b) shows that when the 90% cold-worked sample is annealed at  $300^\circ\text{C}$  for 1h, the texture components are nearly  $(023) [\bar{3}3\bar{2}] + (111) [\bar{u}vw]$  type. Since, the type of texture developed in case of 90% cold-worked sample annealed at  $350^\circ\text{C}$  for 1h [Fig.4.1(c) ] is different from that for 90% cold-worked sample annealed at  $300^\circ\text{C}$  for 1h, [Fig.4.1(b) ], it is not possible to correlate them. In fact, Fig. 4.1(c) shows the development of random texture with one component being close to  $(225) [\bar{5}5\bar{4}]$  type . The texture developed in 60% cold-deformed sample annealed at  $350^\circ\text{C}$  for 1h is close to  $(110) (\bar{1}12)$  type [Fig. 4.2(b) ] .

4.2.2 Precipitation treated Samples: (111) pole figure for 90% cold worked sample is shown in Fig. 4.4(a). From the position of the maximum intensity contours it can be inferred that the rolling plane is almost parallel to (111) plane. However, in this case also, it is not possible to find out the indices of rolling-direction. A comparison of Figs. 4.1(a), 4.2(a), 4.3, 4.4(a) and 4.5 shows that the effect of fine precipitate particles upon the tendency for texture formation is negligible. Fig. 4.4(c) shows the (111) pole figure for 90% deformed alloy annealed at 350°C for 1h. It can be said to have developed a random texture with one component being close to (211)  $[11\bar{3}]$  type; moreover the persistence of rolling texture component is obvious. We have found random texture even in the case of a 90% cold-deformed S.T. alloy annealed at 350°C for 1h. Fig. 4.4(b) shows the (111) pole figure for 90% cold-worked alloy, annealed at 300°C for 1h. A texture component (023)  $[33\bar{2}]$  develops. Rolling texture component is still present. Now, it is evident that 90% deformed S.T. alloy annealed at 300°C for 1 h [Fig. 4.1(b)] develops similar kind of texture as that found in 90% deformed P.T. alloy annealed at 300°C for 1h [Fig. 4.4(b)]. However, in the latter case peak intensity is higher, indicating more recrystallization.

Figure 4.5 shows the (111) pole figure for 40% cold-deformed alloy. The texture is very close to (111)  $[uvw]$  type.

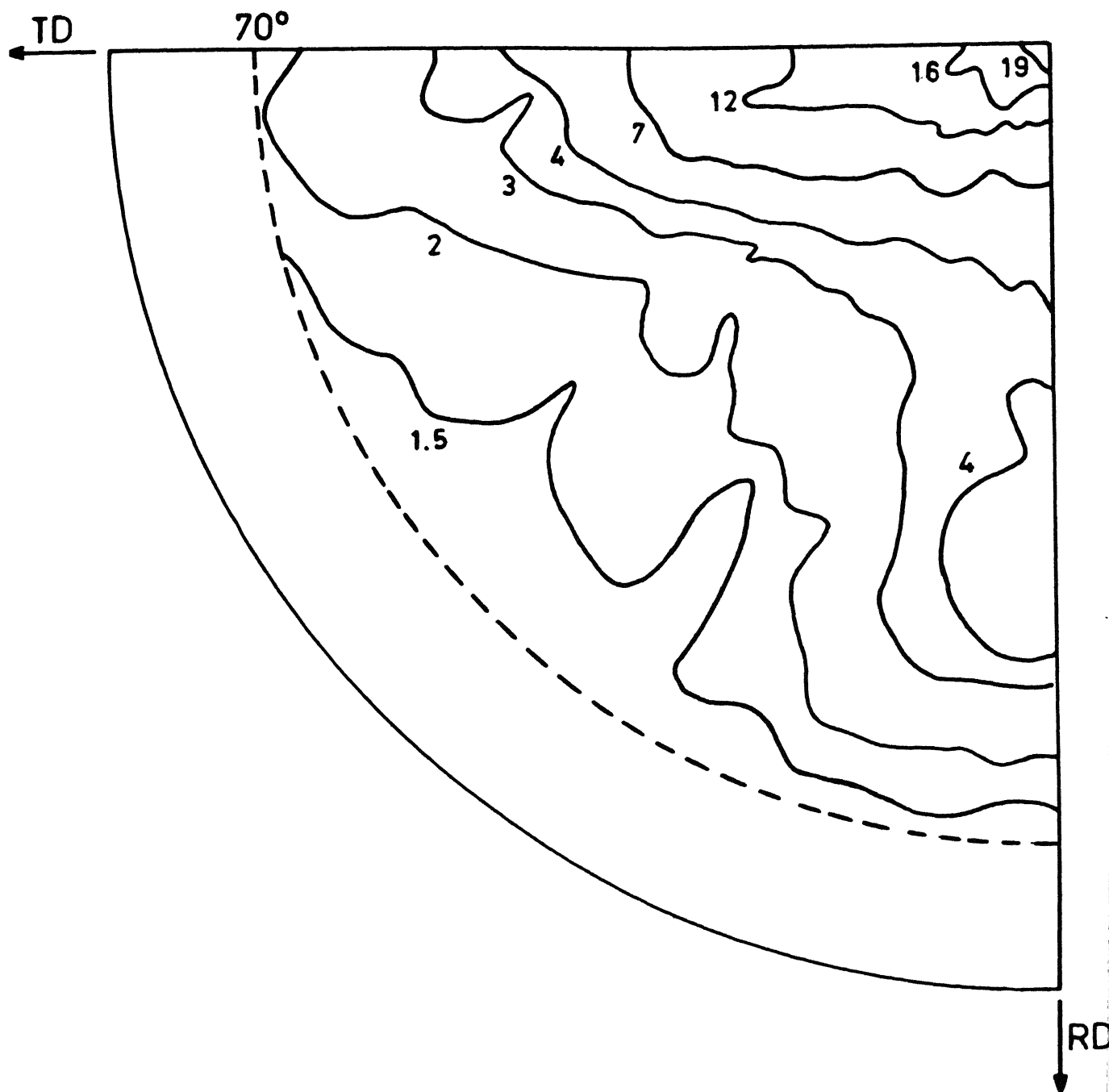


Fig.4.1 (a) (111) pole figure of solution-treated alloy, deformed 90 %.

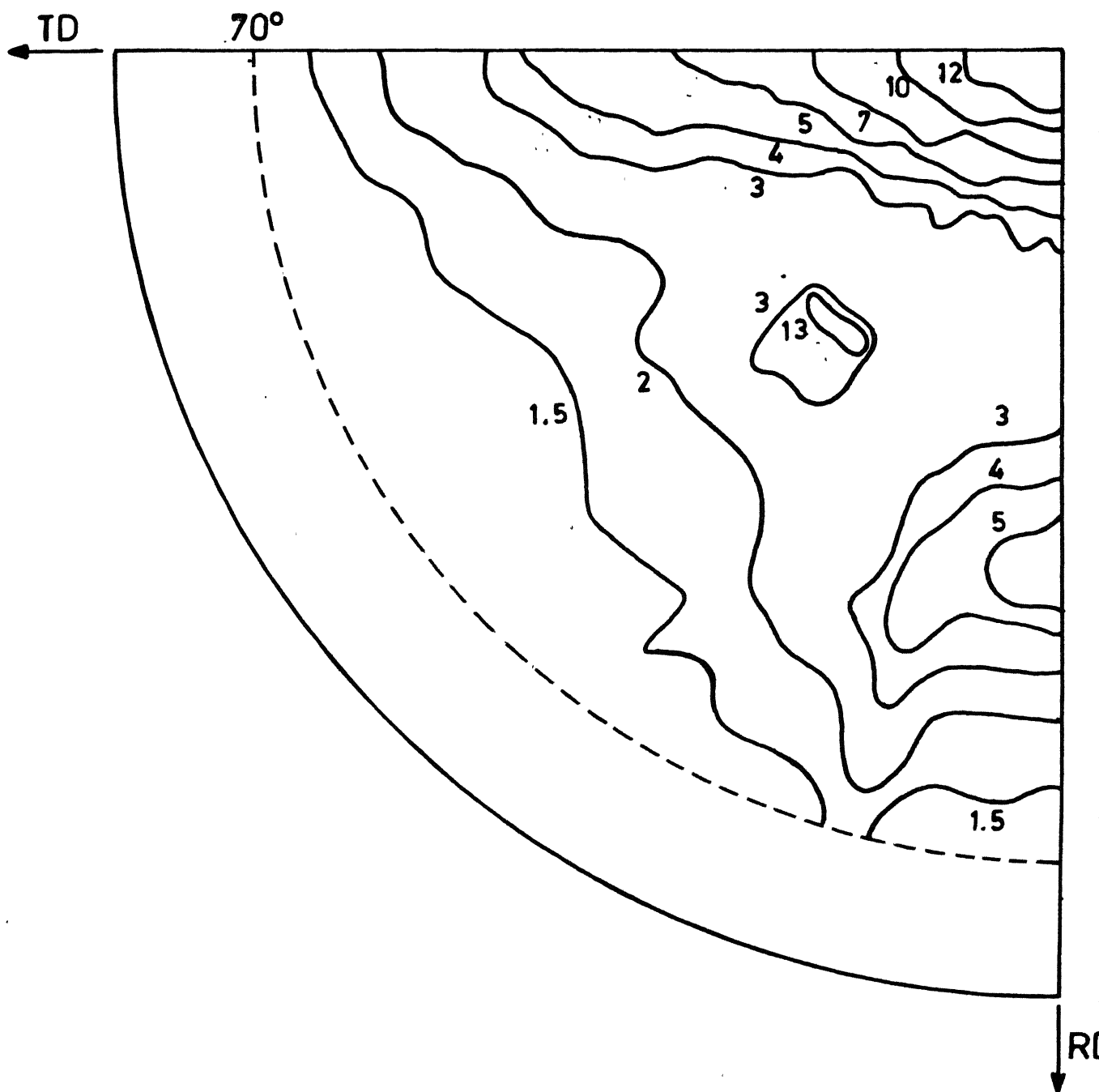


Fig. 4.1(b) (111) pole figure of solution-treated alloy, deformed 90% and then heated to 300°C for 1hr.

92061



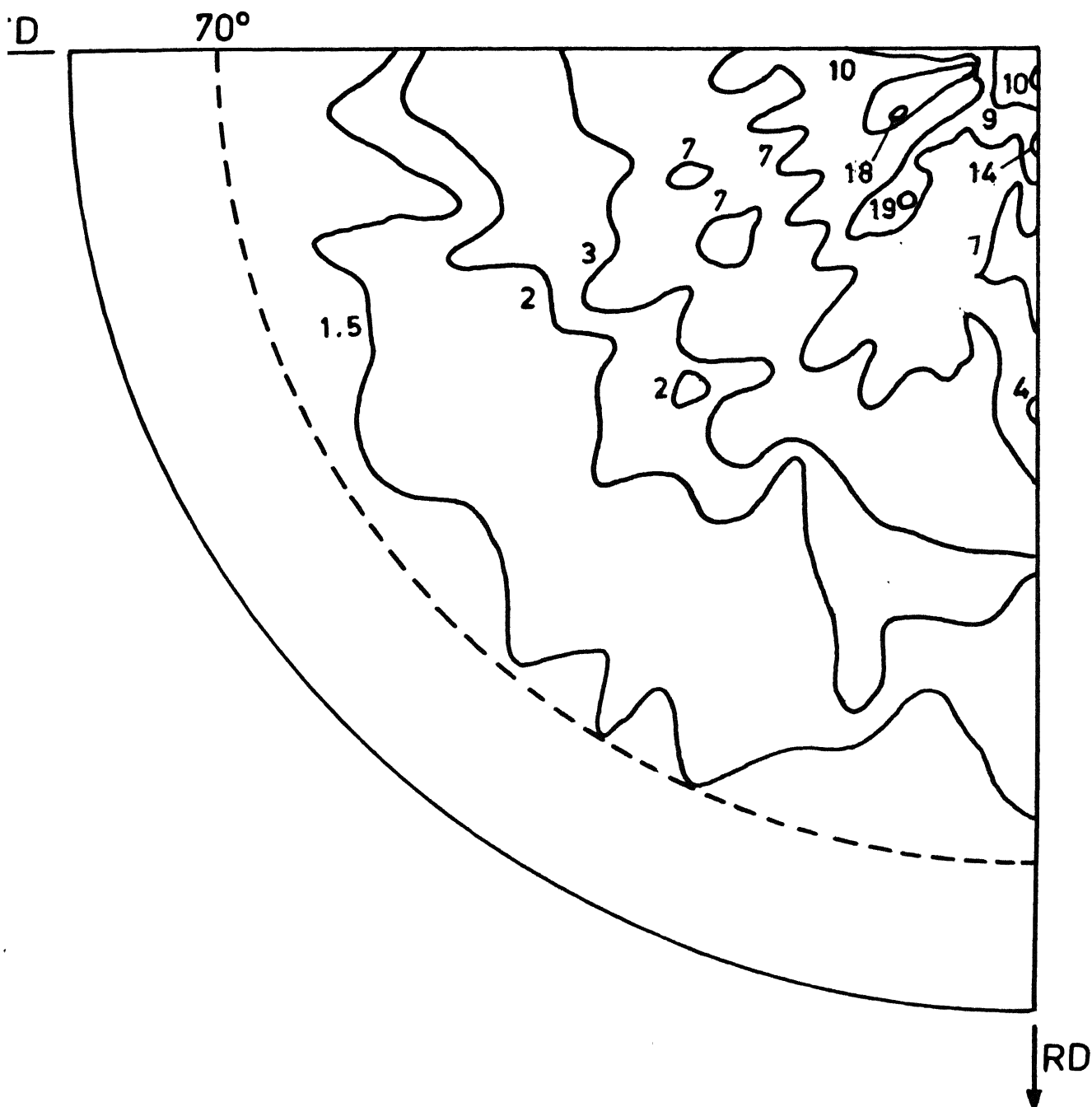


Fig. 4.1(c) (111) pole figure of solution-treated alloy, deformed 90% and then heated to 350°C for 1hr.

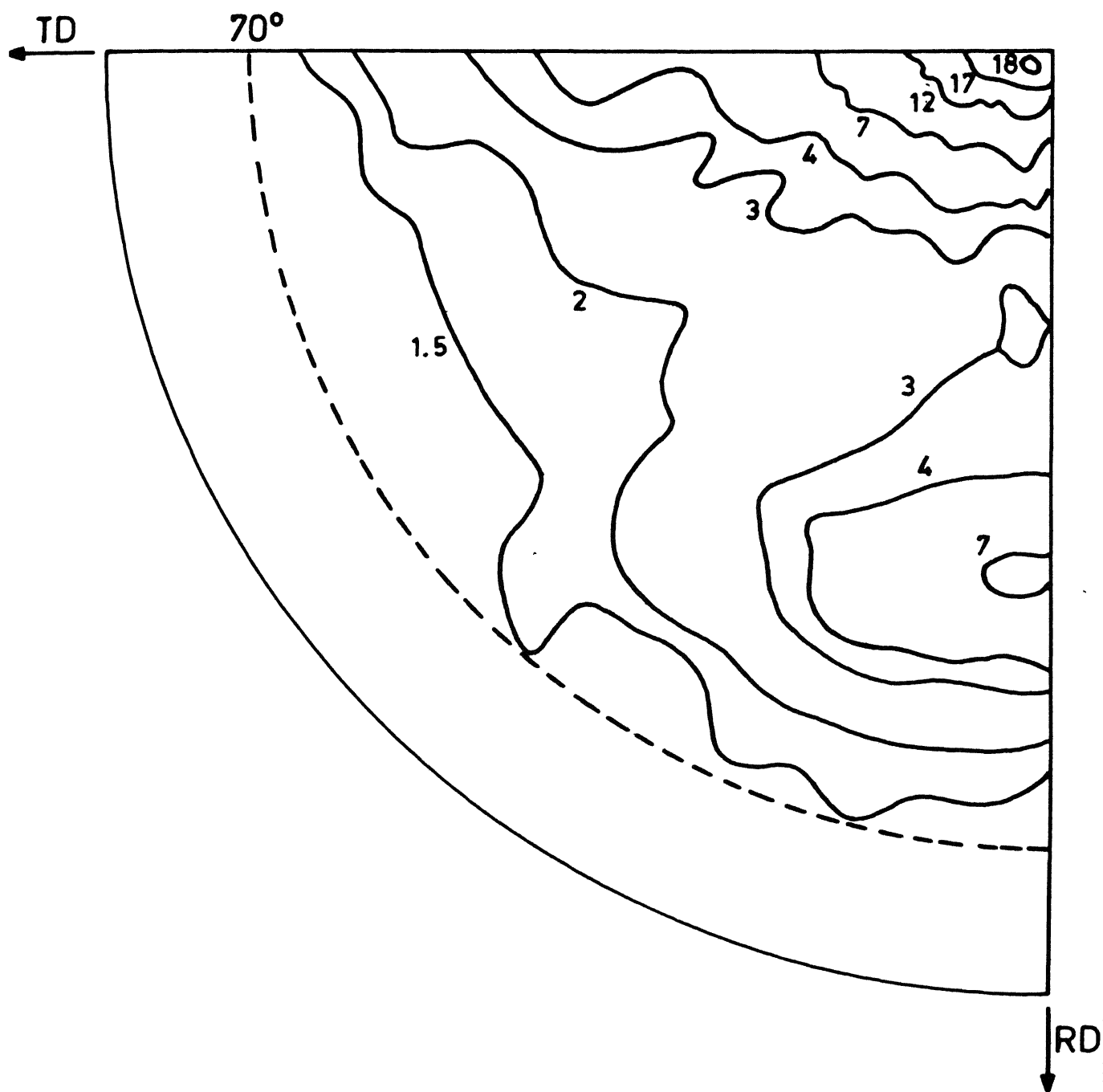


Fig.4.2(a) (111) pole figure of solution-treated alloy, deformed 60% .

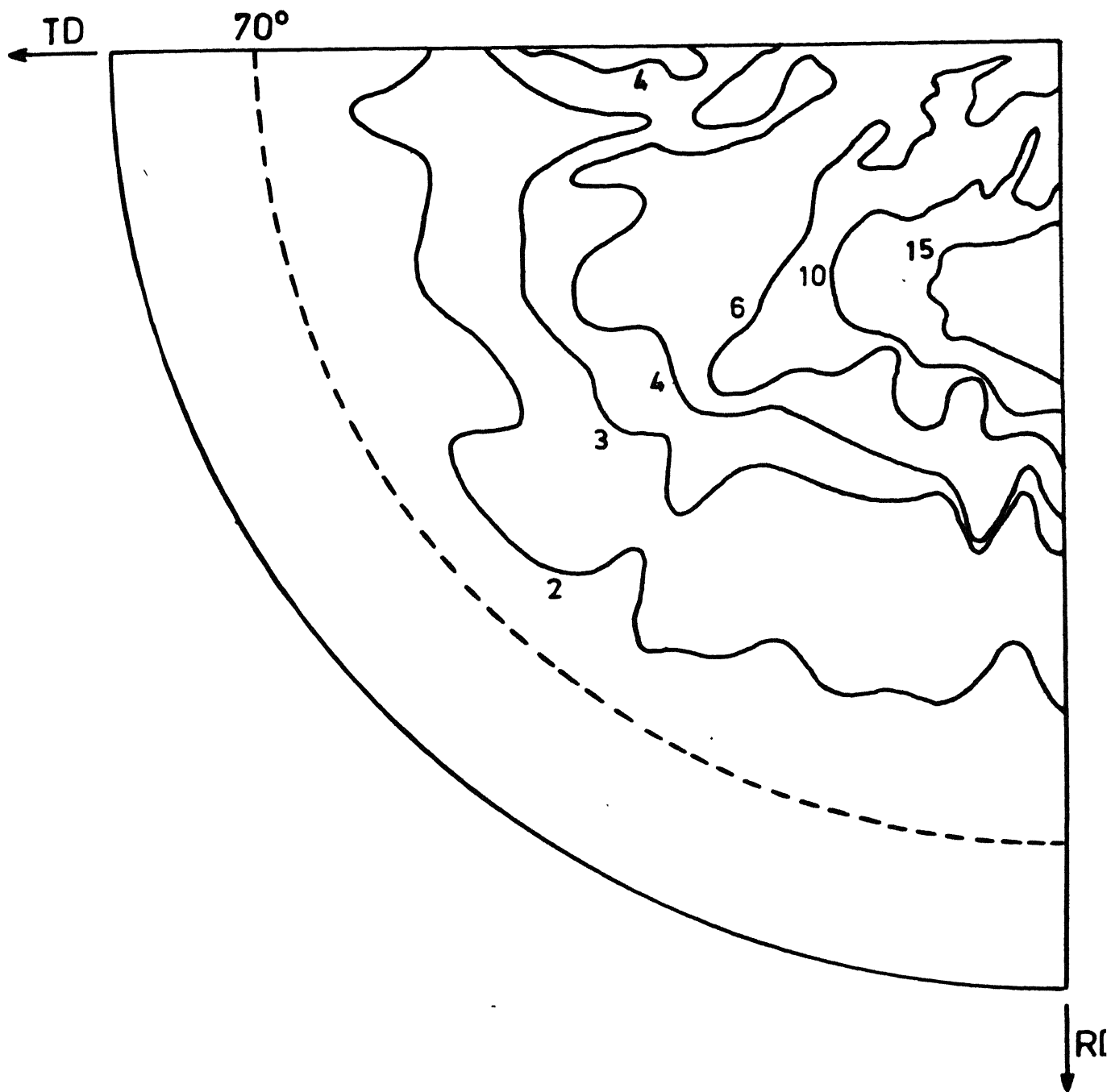


Fig. 4.2(b) (111) pole figure of solution-treated alloy, deformed 60% and then heated to 350°C for 1hr.

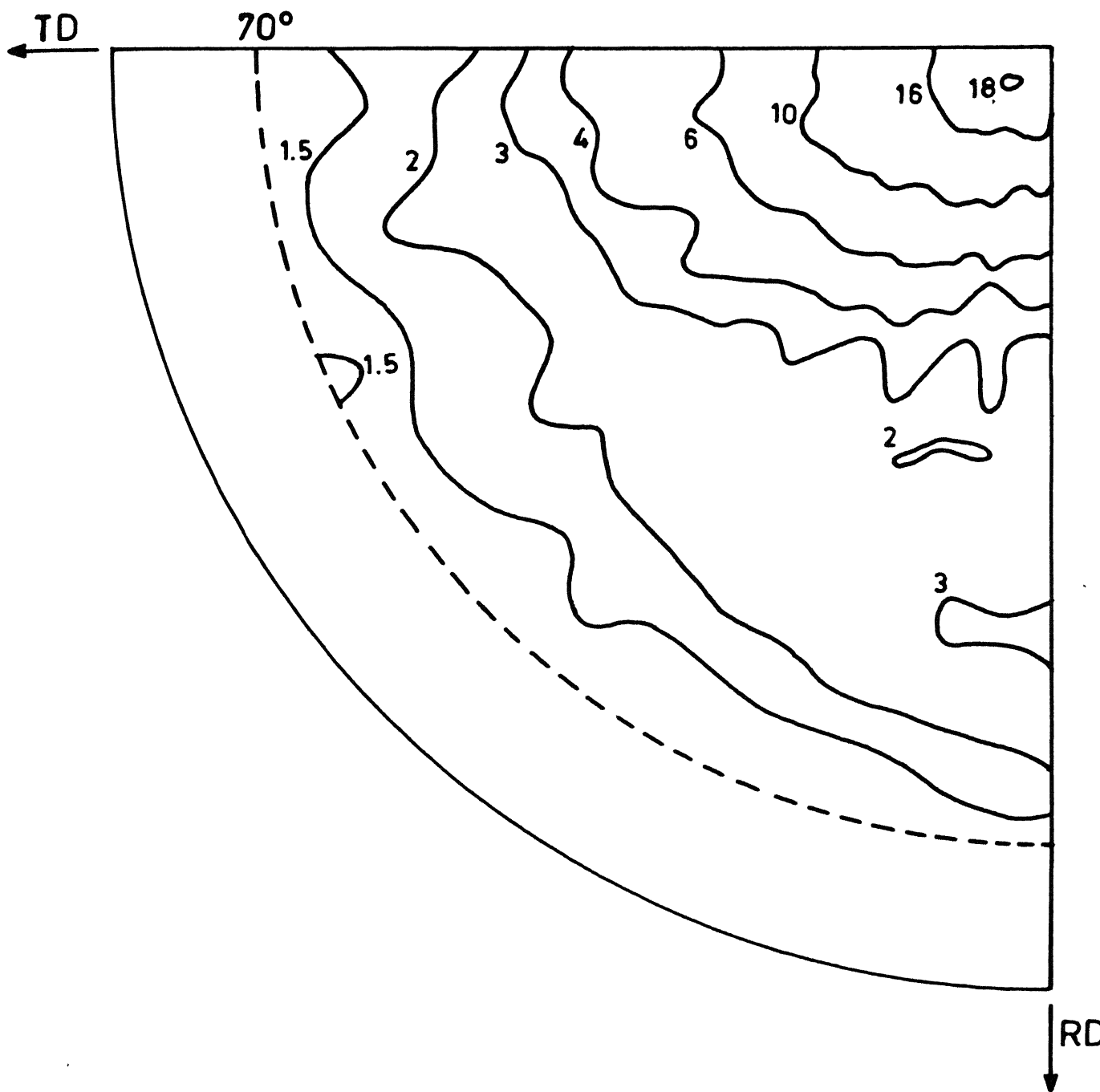


Fig. 4.3 (111) pole figure of solution-treated alloy, deformed 40%.

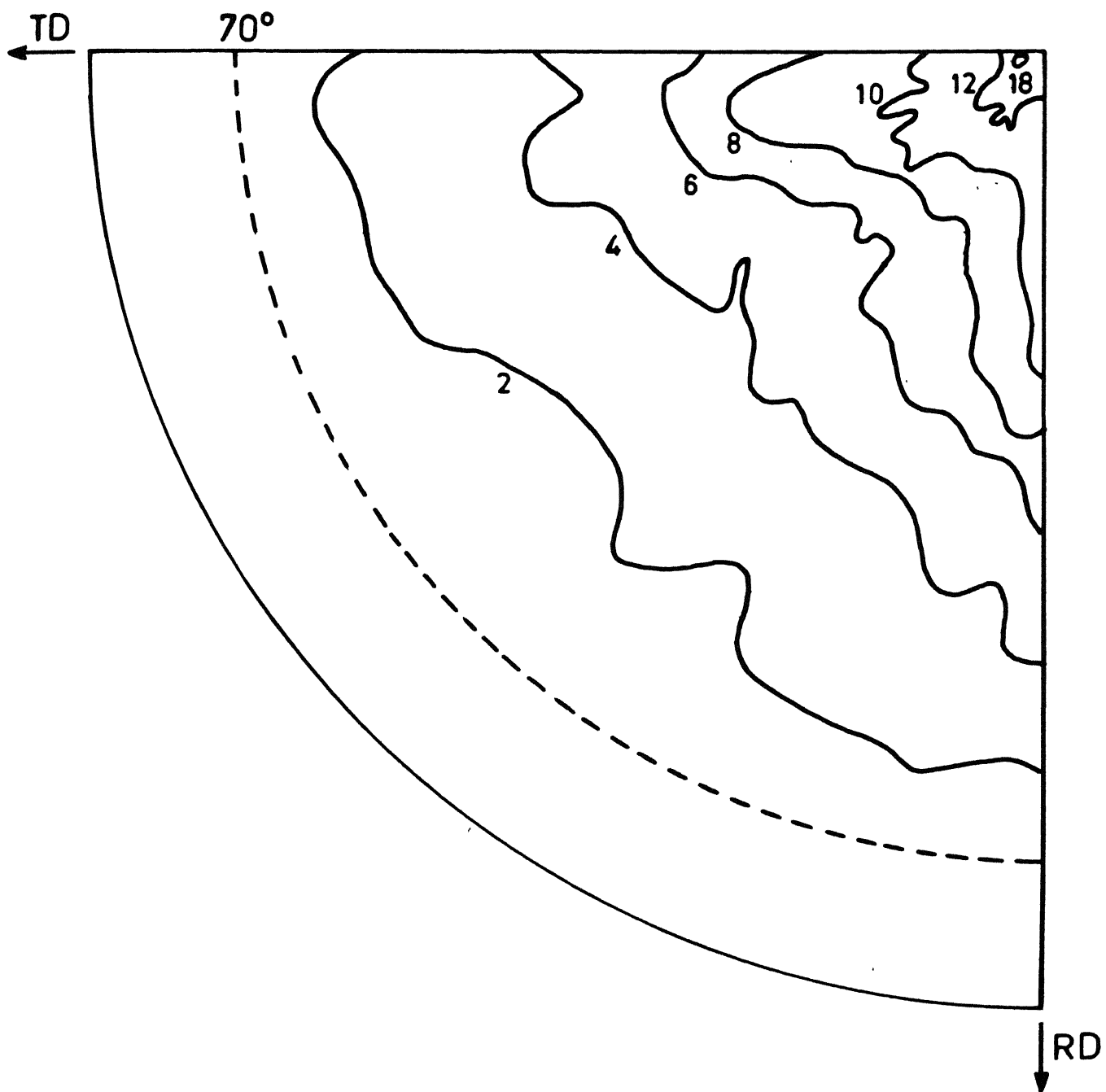


Fig.4.4(a) (111) pole figure of precipitation -treated alloy , deformed 90% .

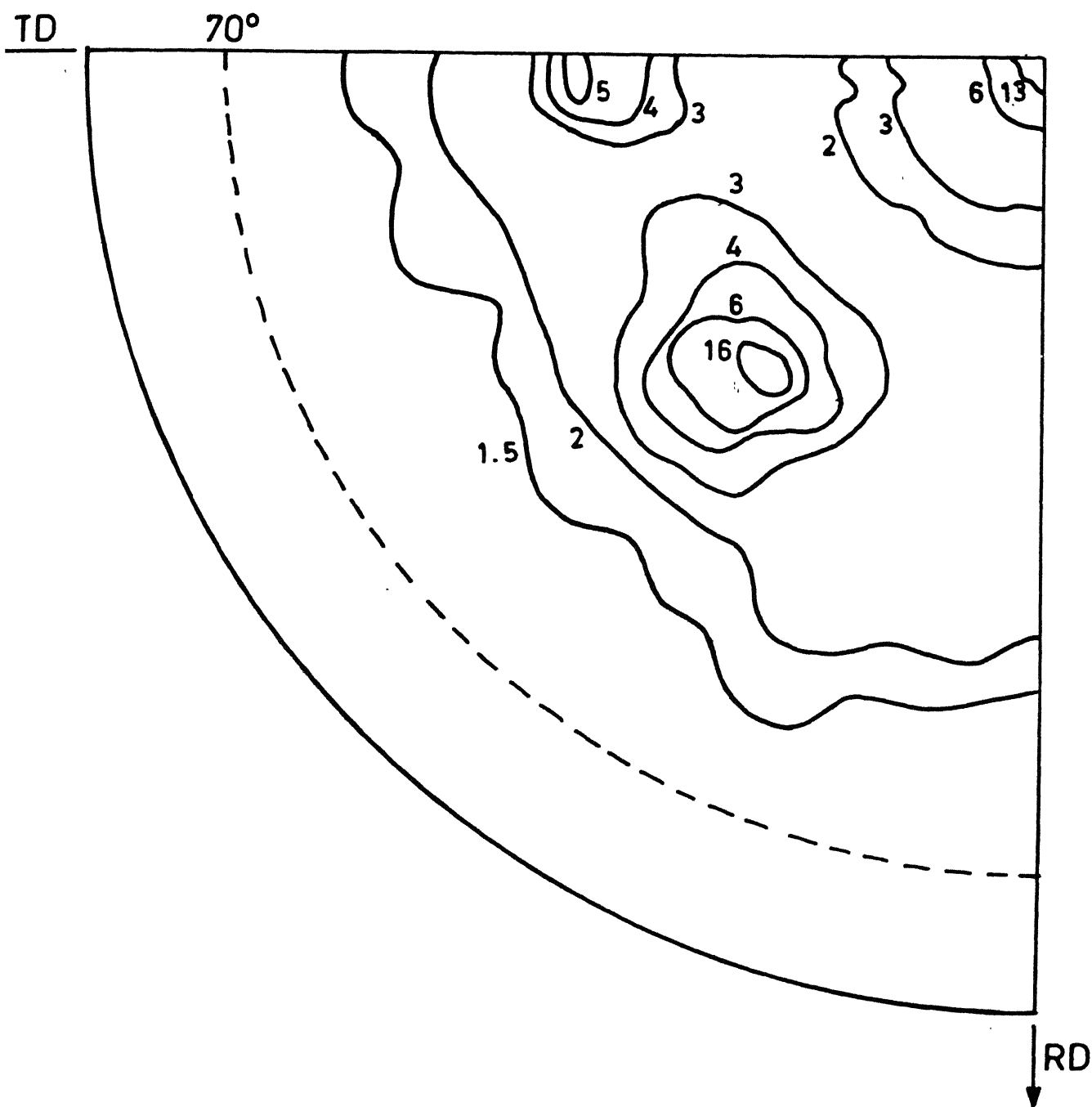


Fig. 4.4(b) (111) pole figure of precipitation-treated alloy, deformed 90% and then heated to 300°C for 1hr

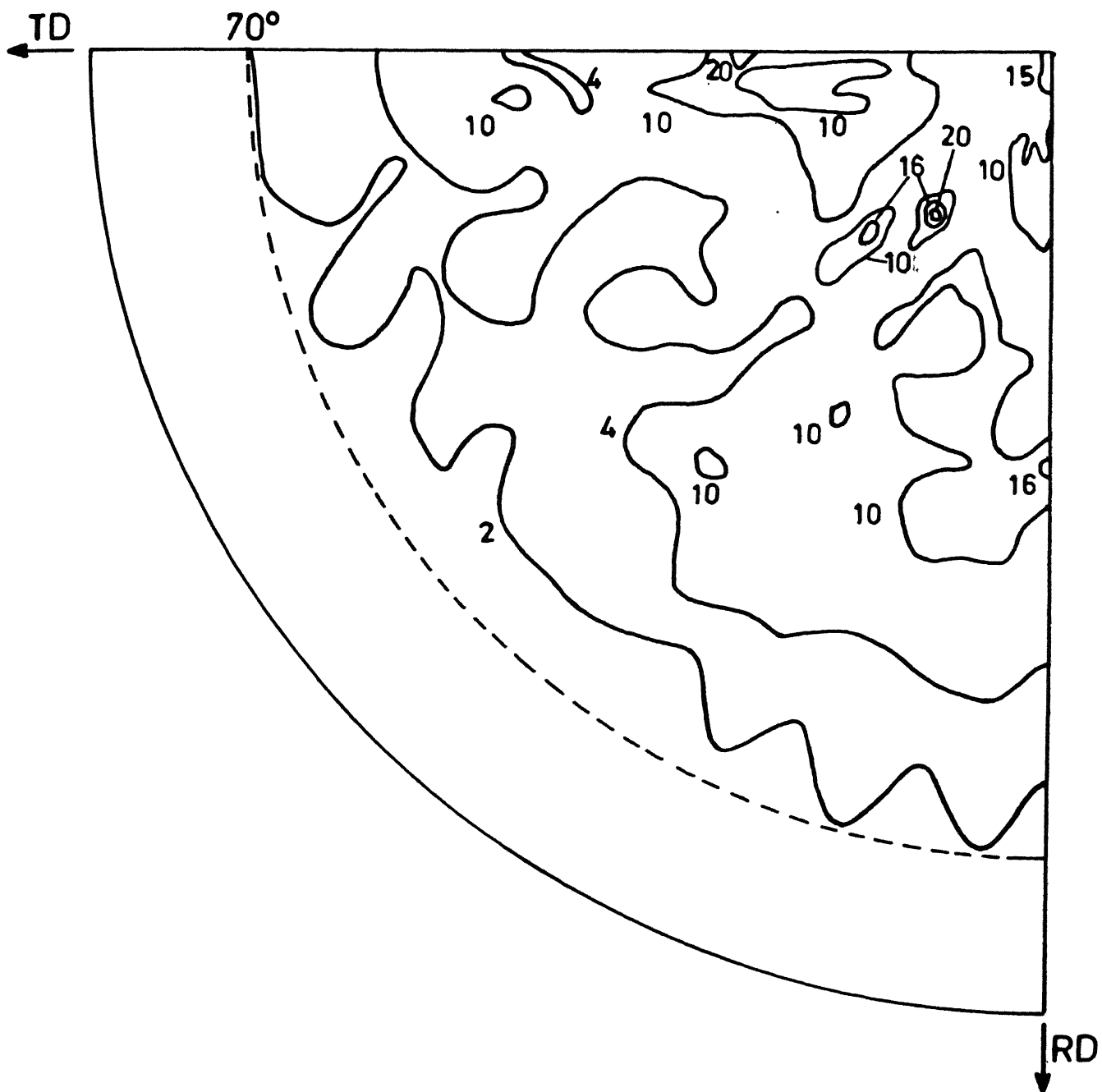


Fig. 4.4 (c) (111) pole figure of precipitation treated alloy, deformed 90% and then heated to 350°C for 1hr

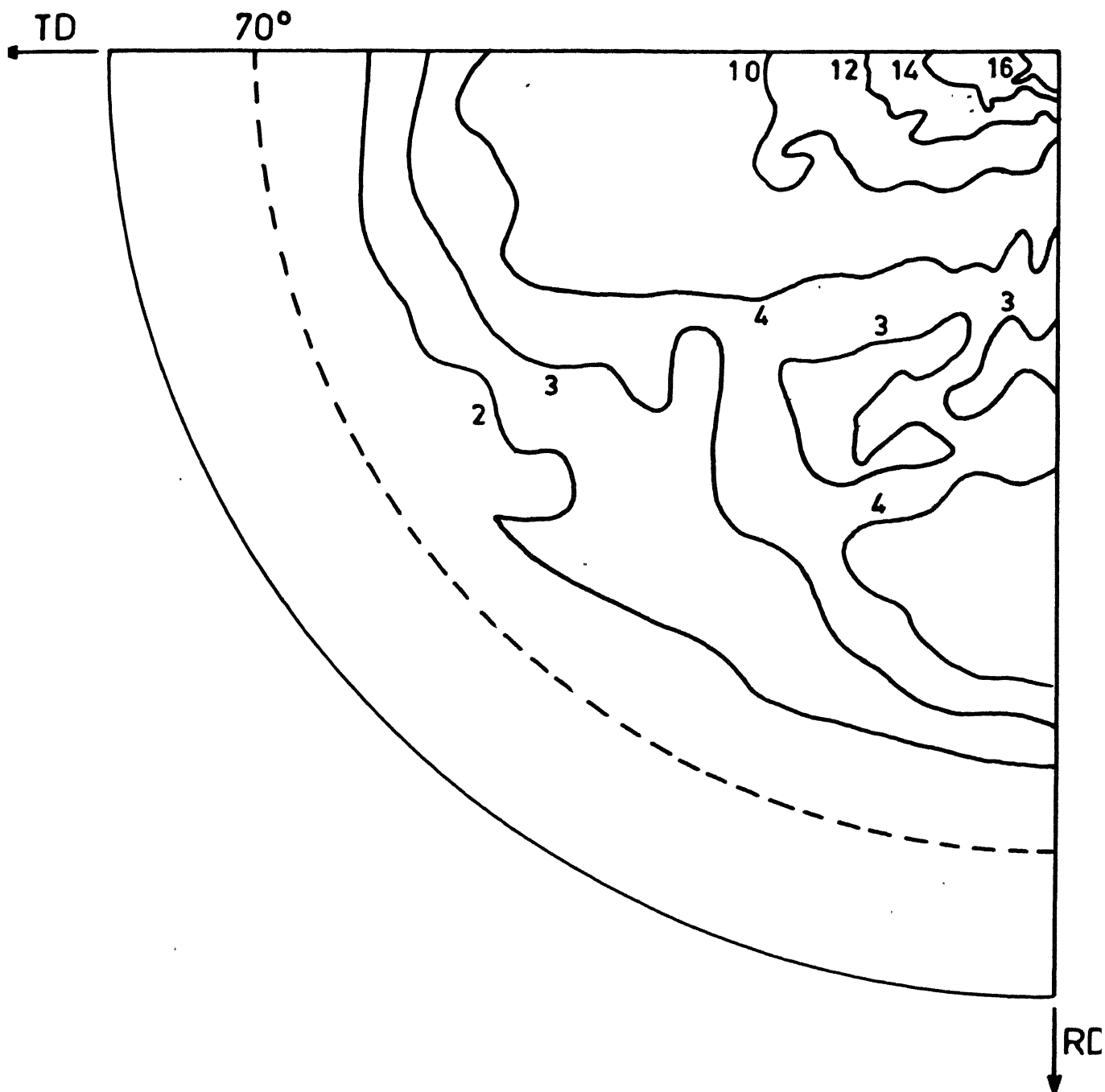


Fig.4.5 (111) pole figure of precipitation-treated alloy, deformed 40%.

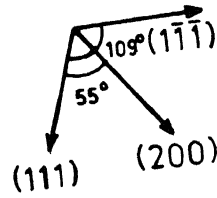


### 4.3 Electron Microscopic Studies

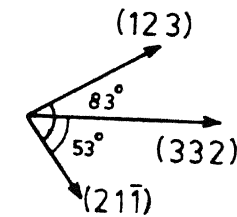
Electron microscopic studies have been carried out on the cold-worked as well as annealed samples for both the solution-treated and the precipitation-treated alloys. The results obtained are discussed below.

4.3.1 Nature of Insoluble Particles: A number of selected area electron diffraction patterns were obtained from primary insoluble particles (Figs. 4.6 to 4.9) after subjecting the alloy to various thermal and mechanical treatments. It is evident that annealing the cold-worked alloys at various temperatures has practically no effect upon the particles; in fact they do not dissolve even after solution-treatment at 620°C for 24 h. The electron diffraction patterns were unambiguously indexed on the basis of the 'd' spacings of  $\text{Al}_{12}(\text{Fe}, \text{Mn})_3\text{Si}$ . It has b.c.c. structure with a lattice parameter of 12.65 Å. The interplanar-spacings for this phase have been furnished in Table I, Appendix I. All the diffraction patterns were, however, checked on the basis of the d-spacings of the other possible phases in the Al-Mn system.  $G_1$ -phase (B.C.C.  $a = 7.533 \text{ Å}$ ),  $G'$  - phase (simple cubic,  $a = 12.75 \text{ Å}$ ),  $\text{MnAl}_6$ -phase (c-centered orthorhombic,  $a = 6.504 \text{ Å}$ ,  $b = 7.555 \text{ Å}$ ,  $c = 8.864 \text{ Å}$ ).

4.3.2 Microstructural Studies: A number of micrographs

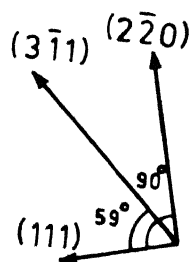
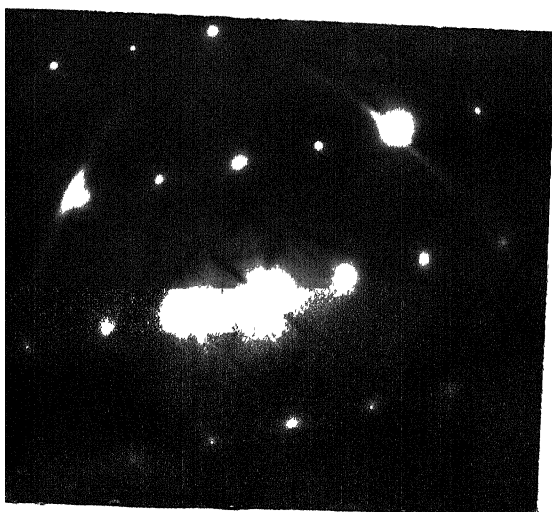


(a)  
300°C, 1 h ;  $\vec{B} [01\bar{1}]$



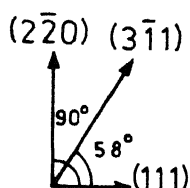
(b)

300°C, 1h. ;  $\alpha\text{-Al}_{12}(\text{Fe}, \text{Mn})_3\text{Si}$ ;  $\vec{B} [573]$

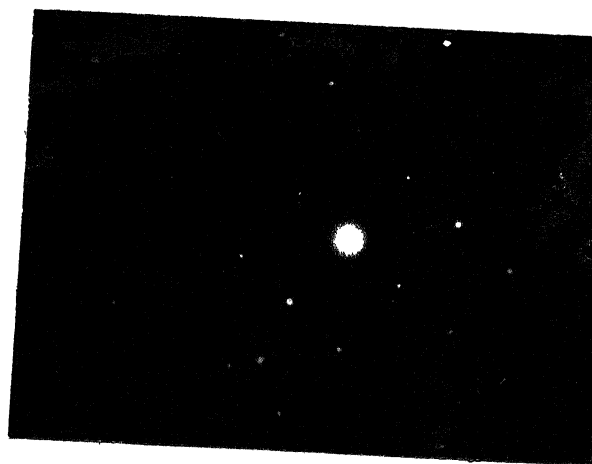
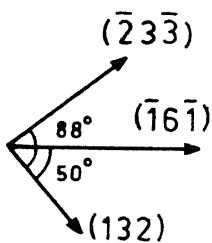


(c)  
350°C, 1h ;  $\vec{B} [\bar{1}12]$

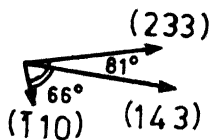
Fig. 4.6 : Diffraction patterns from solution-treated 3004 alloy cold worked 90% and then annealed  
(a) from matrix; (b) from insoluble; (c) from matrix.



(a)  
250°C, 1 h ;  $\vec{B}[11\bar{2}]$



(b)  
250°C, 1 h ;  $\alpha\text{-Al}_{12}(\text{Fe,Mn})_3\text{Si}$ ;  
 $\vec{B}[\bar{15} \bar{1}9]$



(c)  
250°C, 1 h ;  $\alpha\text{-Al}_{12}(\text{Fe,Mn})_3\text{Si}$ ;  $\vec{B}[33\bar{5}]$

Fig.4.7 : Diffraction patterns from solution treated 3004 alloy cold worked 60% and then annealed  
(a) from matrix; (b) and (c) from insoluble.

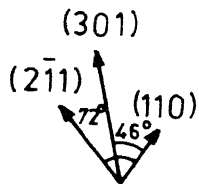
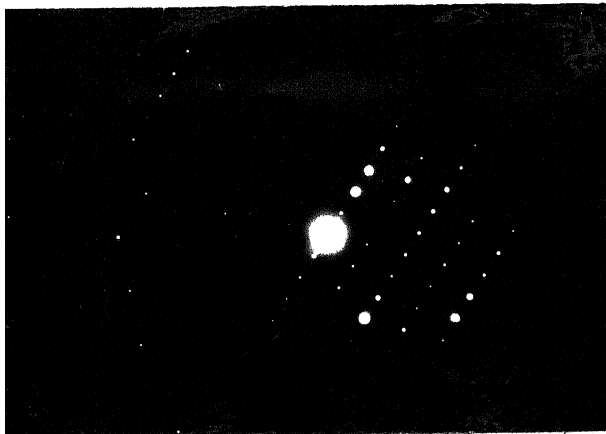


Fig.4.7 (d)  
 $250^{\circ}\text{C}, 1 \text{ h} ; \alpha\text{-Al}_{12}(\text{Fe}, \text{Mn})_3\text{Si},$   
 $\vec{B} [1\bar{1}\bar{3}]$

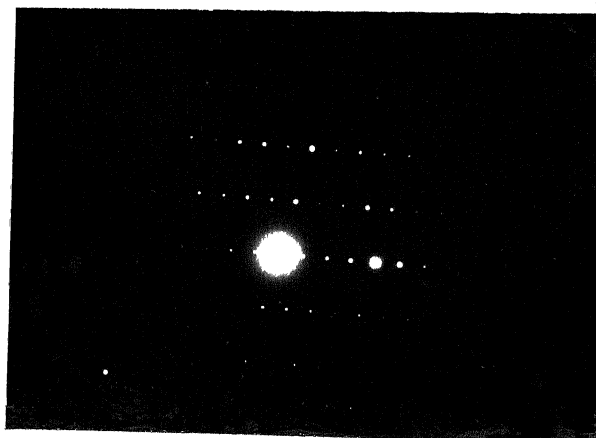
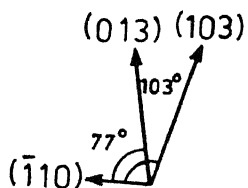


Fig. 4.7 (e)  
 $250^{\circ}\text{C}, 1 \text{ h} ; \alpha\text{-Al}_{12}(\text{Fe}, \text{Mn})_3\text{Si}; \vec{B} [\bar{3}\bar{3}\bar{3}]$

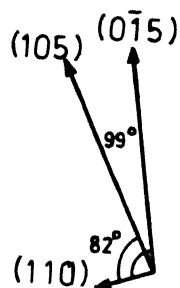
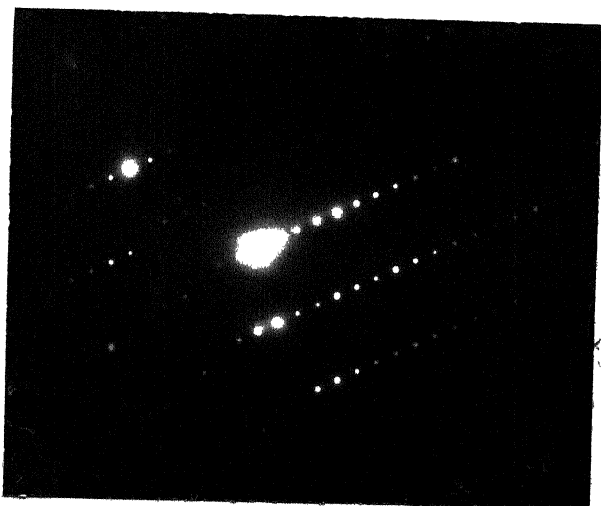
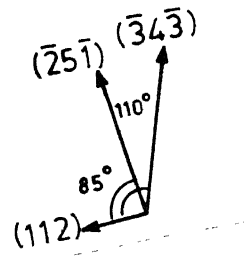
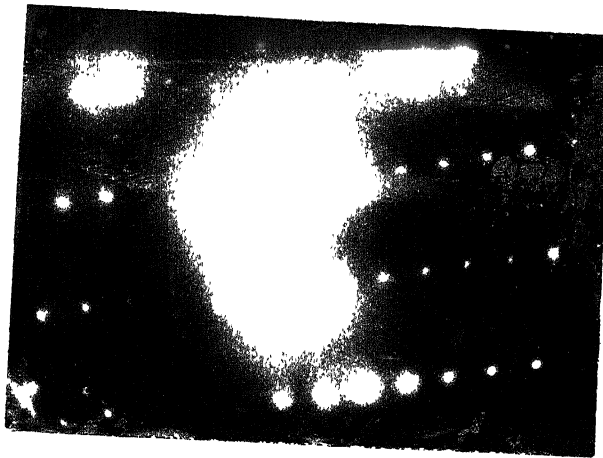


Fig. 4.8  
 $\alpha\text{-Al}_{12}(\text{Fe}, \text{Mn})_3\text{Si}; \vec{B} [\bar{5}\bar{5}\bar{1}]$

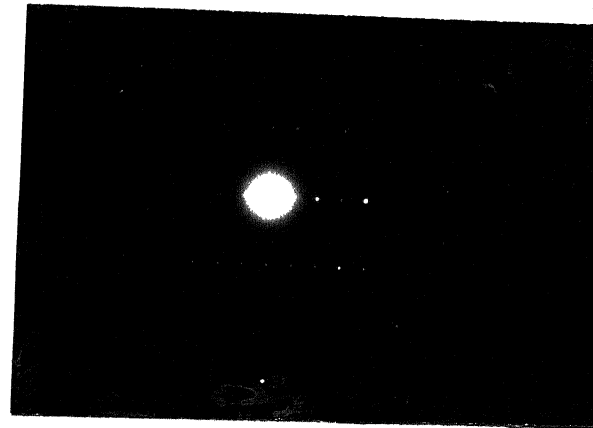
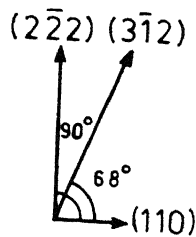
Fig.4.7 (d) & (e) : From insolubles

Fig.4.8 : Diffraction pattern from insoluble of solution treated alloy, cold worked 90%.



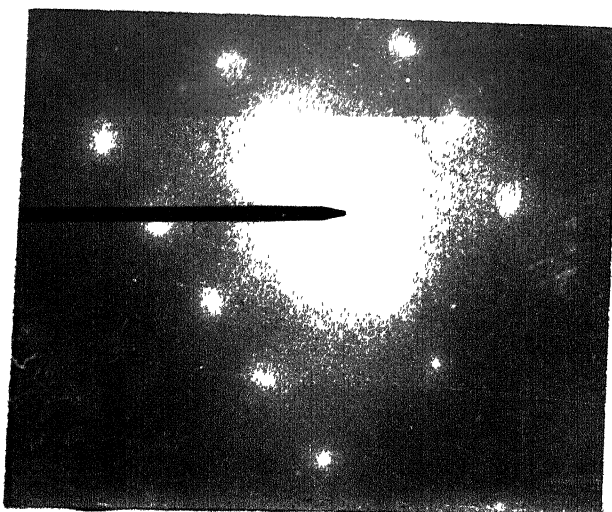
(a)

$250^{\circ}\text{C}, 1 \text{ h}; \alpha\text{-Al}_{12}(\text{Fe}, \text{Mn})_3\text{Si}, \vec{B}[113\bar{7}]$



(b)

$\alpha\text{-Al}_{12}(\text{Fe}, \text{Mn})_3\text{Si}; \vec{B}[1\bar{1}\bar{2}]$



(c)

$250^{\circ}\text{C}, 1/2 \text{ h}; \vec{B}[1\bar{1}\bar{2}]$

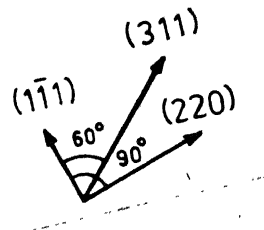


Fig.4.9 : Diffraction patterns from 3004 alloy  
 (a) From insoluble of the as-received alloy, cold worked 97%; and then annealed at  $250^{\circ}\text{C}$  for 1 h;  
 (b) From insoluble of the as-received alloy, cold worked 97%; (c) From matrix of the as-received alloy

obtained in both solution-treated as well as precipitation treated conditions. Further more a few micrographs of deformed and annealed states from the as-received material have also been presented. A brief account of the results is given below.

4.3.2.1 As-received Samples: The micrographs of the as-received alloy cold-worked 97%, have been presented in Figs. 4.19(a), (b) and (c)). In Fig. 4.19(a), the elongated cell-structure of the deformed alloy is shown by mark 'A'. Every et al. (23) observed that the cell-shape was a function of the grain-orientation, being elongated for  $\{110\}$  (high-energy) and equiaxed for  $\{100\}$  (low energy) orientations. Figs. 4.19(b) and (c) show the deformation structure around insoluble particles [Mark 'B' in Fig. 4.19(b) and Mark 'C' in Fig. 4.19(c)]. In Fig. 4.19(b) also, we see elongated cell structure in region slightly away from the insoluble particle [Mark 'B' in Fig. 4.19(b)]. The average cell-size in the general area was measured to be about  $0.15 \mu\text{m}$ .

The cold worked as-received material was annealed at  $250^{\circ}\text{C}$ . One part was annealed for 30 minutes while the other part was annealed for 60 minutes. Fig. 4.20 show the electron micrographs for  $250^{\circ}\text{C}$ , 30 mts treatment. A careful investigation of the micrographs in Fig. 4.20 makes it clear that annealing at  $250^{\circ}\text{C}$  for  $1/2$  h has hardly

modified the deformed structure in the general area. Well defined cell-structures are evident in Figs. 4.20(a) and (c). However, we see a few partially recovered grains in the deformation zone around an insoluble particle [Mark 'A' in Fig. 4.20].

The micrographs for one hour annealing treatment at 250°C have been presented in Fig. 4.21. In both Figs. 4.21(a) and (b) we see the appearance of high angle grain boundaries [Mark 'A' in Fig. 4.21(a) and Mark 'B' in Fig. 4.21(b)]. This indicates the onset of recrystallization.

#### 4.3.2.2 Solution-treated Samples

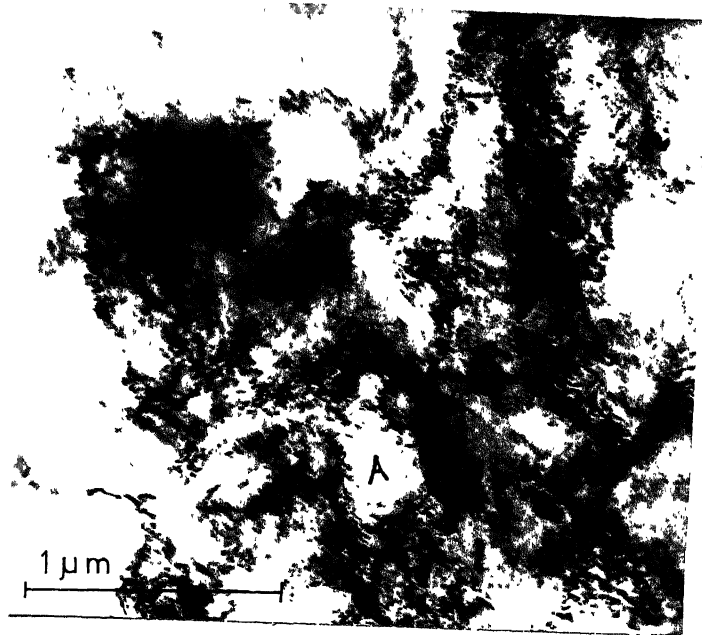
One part of the solution treated samples was given 90% deformation, while the other part was deformed to 60%; deformation being imparted by cold-rolling in both the cases. The micrographs for 90% cold-deformed alloy are shown in Figs. 4.10(a) and (b). In Fig. 4.10(a) dislocation tangles are seen in the deformation zone around a primary insoluble of size  $\approx 0.29 \mu\text{m}$ . Weak cell structure ( $\approx 0.25 \mu\text{m}$ ) is visible in the proximity of the particle, whereas a well-defined cell structure [Mark 'A' in Fig. 4.10(a)] with a much higher dislocation-density at the cell boundary, is seen slightly away from the particle. This observation is in agreement with the results obtained by Gatto et al. (28). In Fig. 4.10(b), an

area near the primary insoluble particle [Mark 'B' in Fig. 4.10(b)]. Consisting of a dense distribution of dislocations is shown. No cell structure is found to form in this region. Due to local misfit strains, the cold-working will result in a higher dislocation density around the large particles than in the surrounding matrix. Hence, on subsequent annealing, this region will act as a potential site for nucleation of new strain-free grains.

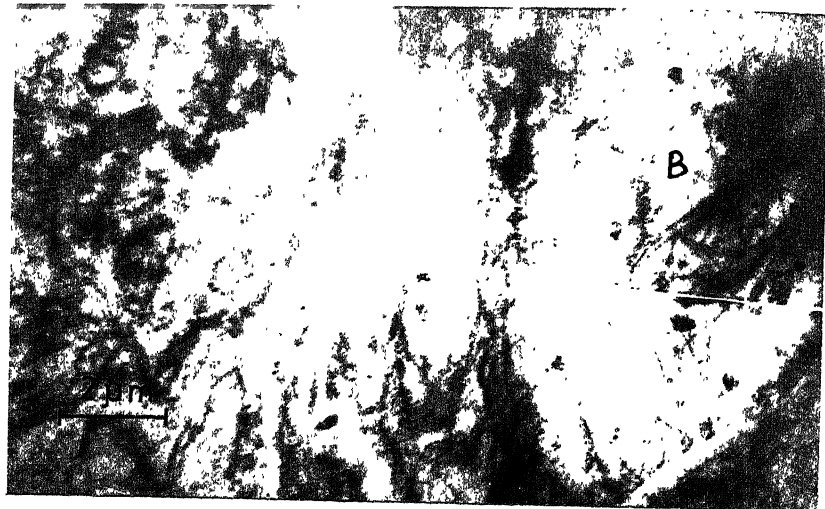
When the cold-worked sample is heated to 300°C for 1h (Fig. 4.11), there is some evidence for the onset of recovery and no evidence for the initiation of recrystallization. Moreover, it is not possible to detect any precipitate.

The micrographs for the alloy, annealed at 350°C for 1h, are shown in Fig. 4.12. Recrystallization is complete. It is clear from Figs. 4.12(a) and (b), that at 350°C both recrystallization and precipitation occur simultaneously. In Fig. 4.12(a), we see two types of precipitate distribution. Large widely spaced precipitates, probably sub-boundary particles ( $\approx 1.2 \mu\text{m}$ ) are ellipsoidal; some are globular in shape. Fine, closely-spaced particles ( $\approx 0.02 \mu\text{m}$ ) are globular in shape. Precipitate density is in the range  $0.43 \times 10^{19} - 1.438 \times 10^{19} / \text{m}^3$ . Fig. 4.12(b) represents a typical high angle boundary in a general region. Precipitates have formed inside the grains and on the boundary.





(a)



(b)

- Fig.4.10 : Microstructures of solution treated alloy, cold worked to 90%.
- (a) bright-field image of area near an <sup>insoluble</sup> ~~secondary~~ precipitate
  - (b) area near primary insoluble. ⑧

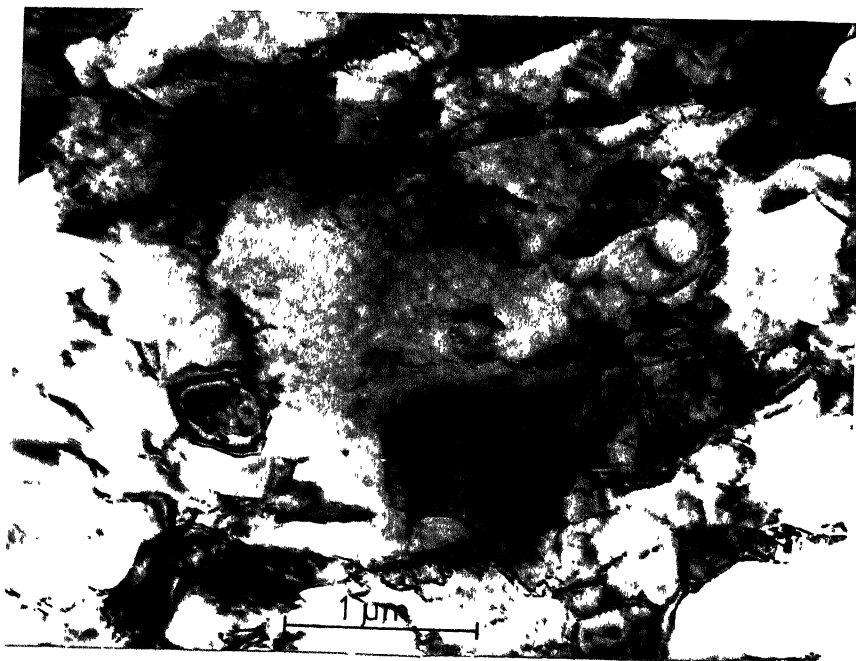
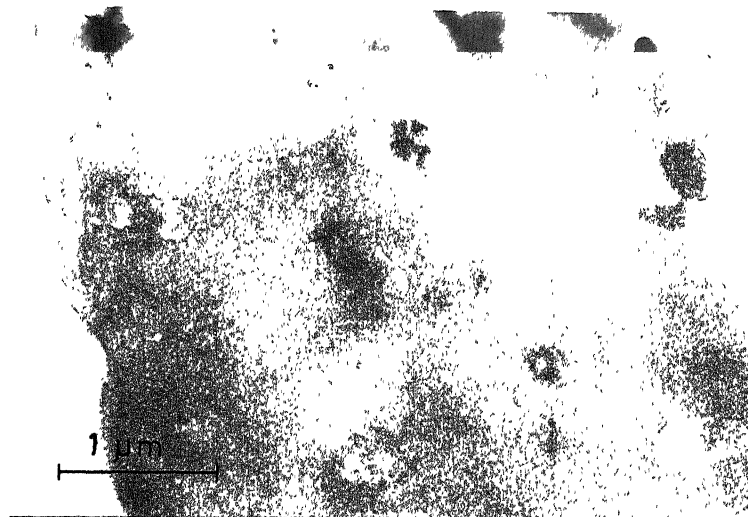
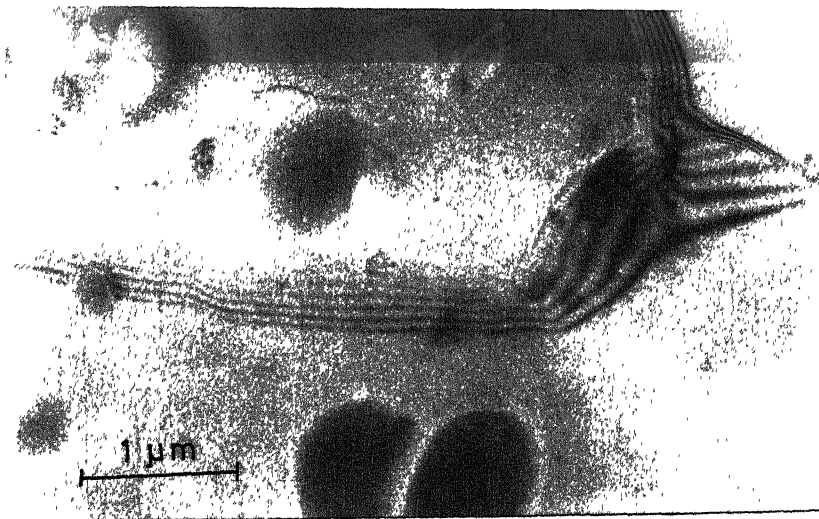


Fig. 4.11 : Microstructures of solution treated alloy cold worked 90%, and then annealed at 300°C for 1 h , showing partially recovered structure.



(a)

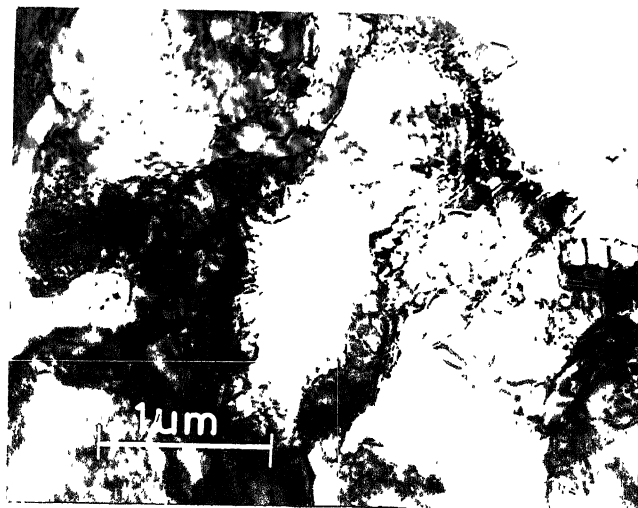


(b)

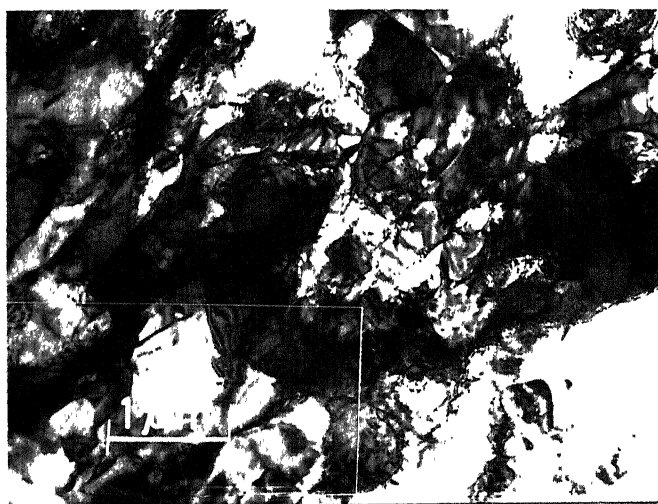
Fig.4.12 : Microstructures of solution treated alloy, cold worked 90%, and then annealed at 350°C for 1 h .  
 (a) recrystallized grain and secondary precipitate  
 (b) precipitates at the grain-boundary and inside the recrystallized grain.



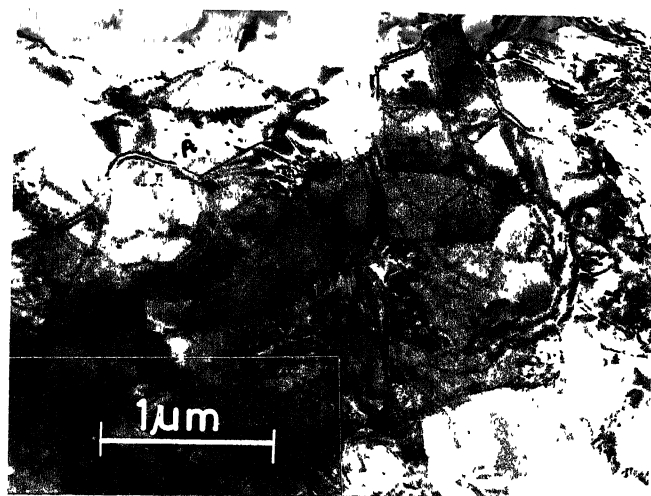
(a)



(b)



(c)



(d)

Fig.4.13 : Microstructures of solution-treated alloy, cold deformed 60% and then annealed at 250°C for 1 h .

- (a) & (b): general areas showing elongated cell-structures
- (c) & (d): partially recovered regions in areas near primary insoluble.

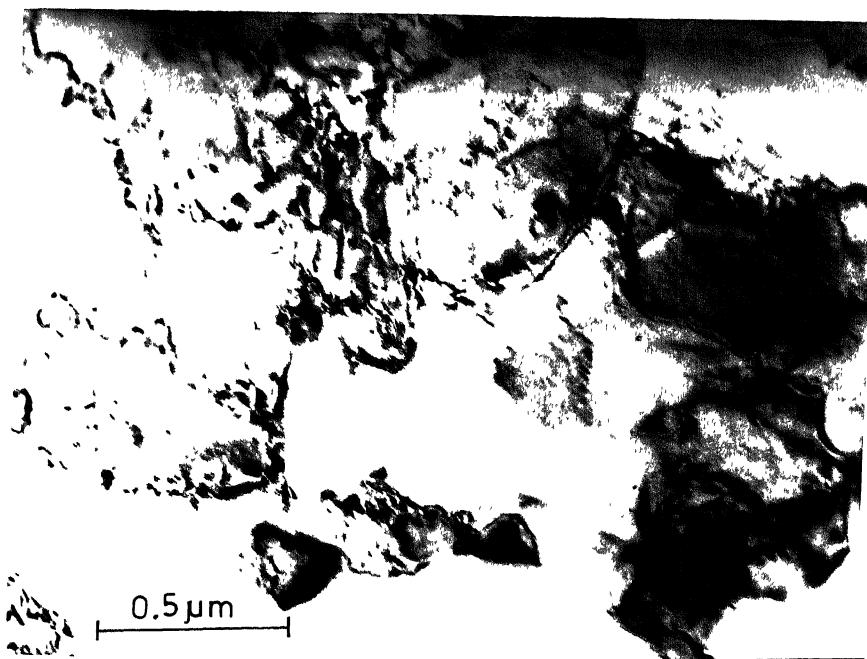
Figures 4.13 (a-d) show electron micrographs of 60% deformed alloy annealed at 250°C for 1h. It is evident that the effect of cold work is still prominent in regions away from primary insolubles (Figs. 4.13 a and b); elongated cells of mean size  $1.3 \mu\text{m}$  are readily visible in the micrographs. The areas shown in Figs. 4.13 (c) and (d) have been taken from regions very near insoluble particle. In these regions recovery has already set in. In Fig. 4.13(d) at 'A' position, few small spots are clearly seen against the white background of the subgrain. These are possibly, secondary precipitate particles, localized at a small region, which have come out of solution during annealing. However, from careful observation of all the micrographs taken for this treatment, it can be inferred that precipitation, if at all occurred at this temperature, is an exception rather than a rule. Since, the features are very small, it is not possible to furnish diffraction information and hence the identification of the nature of the precipitate particles is difficult.

#### 4.3.2.3 Precipitation-treated Samples

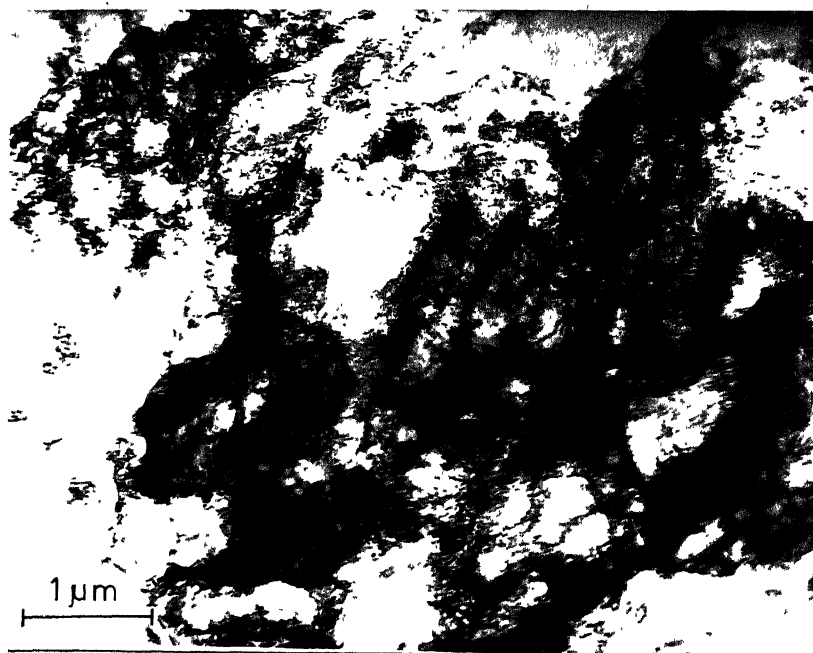
The precipitation-treated samples were deformed to 90% as well as 60%. The average size of precipitate particles was about  $0.2 \mu\text{m}$  whereas the density of precipitate particles was in the range of  $1.38 \times 10^{19} - 2 \times 10^{19} / \text{m}^3$ . The average cell-size is  $1.1 \mu\text{m}$ . Fig. 4.14 shows the

micrographs for 90% deformed samples. Fig.4.14(a) shows clearly discernible cell-structure. However, the average cell structure formed in this case is greater in size than that for an alloy solution-treated only prior to deformation. This observation is quite in agreement with those of others. Actually, stacking fault energy is increased on precipitation; consequently, fault becomes narrow and cross-slip is facilitated. No precipitate particle is seen in Fig.4.14(b). Probably, this micrograph has been taken from a region where precipitation has not occurred. A treatment at 400°C for 12h is not sufficient to effect precipitation to a large extent.

The micrographs for the samples annealed at 300°C for 1h (Fig. 4.15) show that recrystallization process is almost complete near insoluble particles [Fig.4.5(a)], whereas sub-boundary thinning has already started in other areas [Fig. 4.15(b)]. Fig.4.15(a) shows that probably one big grain has formed on annealing, in the region near an insoluble ( $\approx 4.2\mu\text{m}$ ) particle. Actually, the number of recrystallization nuclei formed at a particle, is a function of particle size. For particles in the size range 1-5  $\mu\text{m}$  (24), usually only one grain is nucleated, but at particle larger than  $\sim 10\mu\text{m}$ , multiple nucleation is frequently observed (25). Fig. 4.16 shows the micrographs for 90% deformed alloy annealed at 350°C for 1h. The micrographs show complete evidence of recrystallization after annealing at

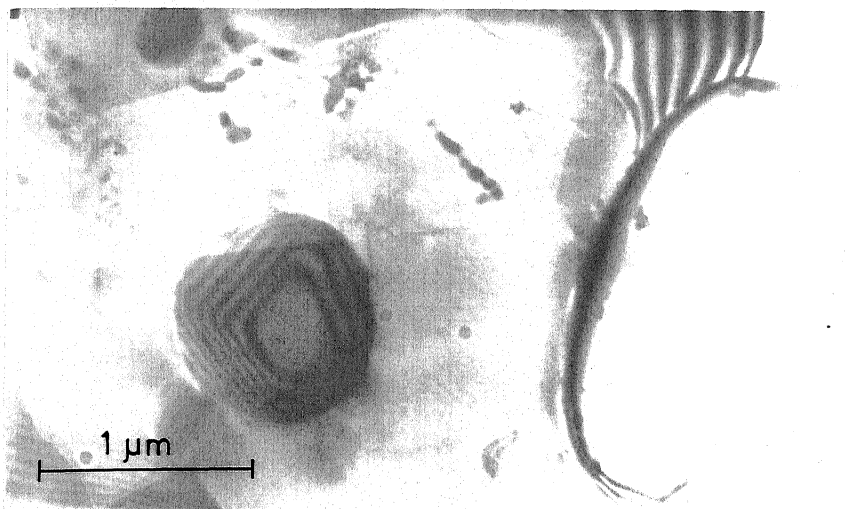


(a)

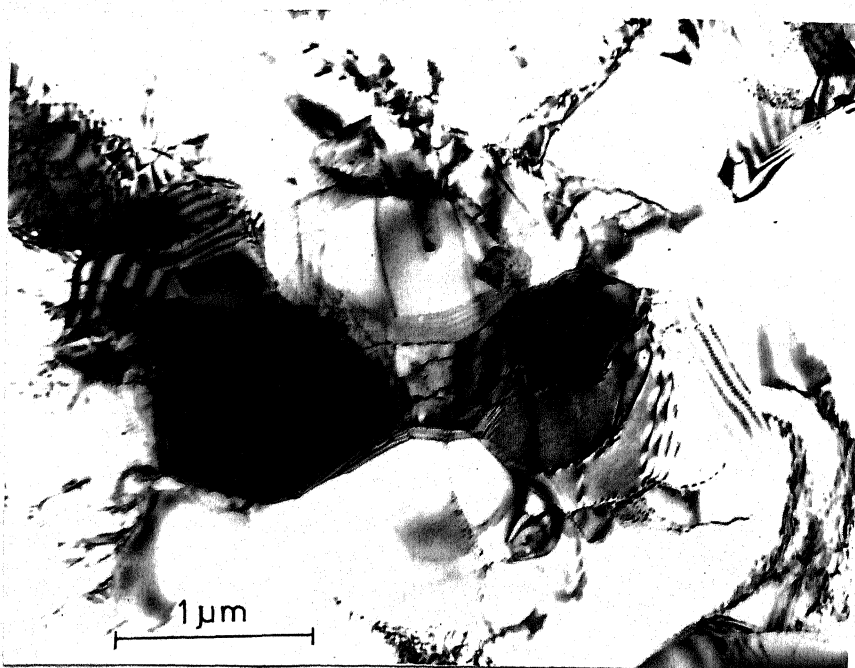


(b)

Fig.4.14 : Microstructure of precipitation-treated alloy, cold worked 90%, showing the formation of cells (a and b).



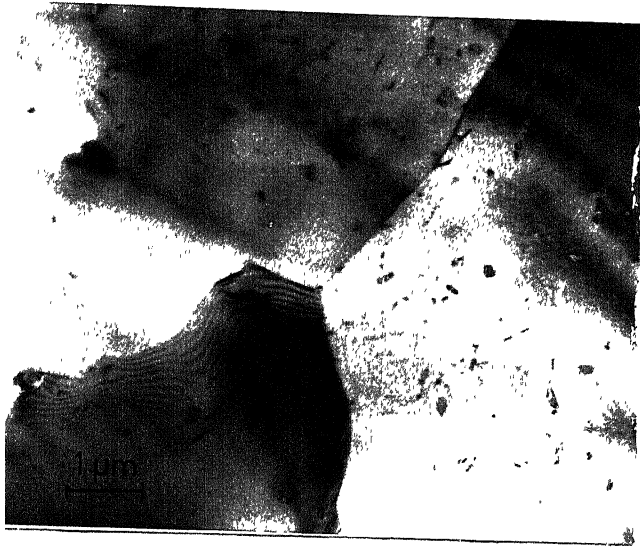
(a)



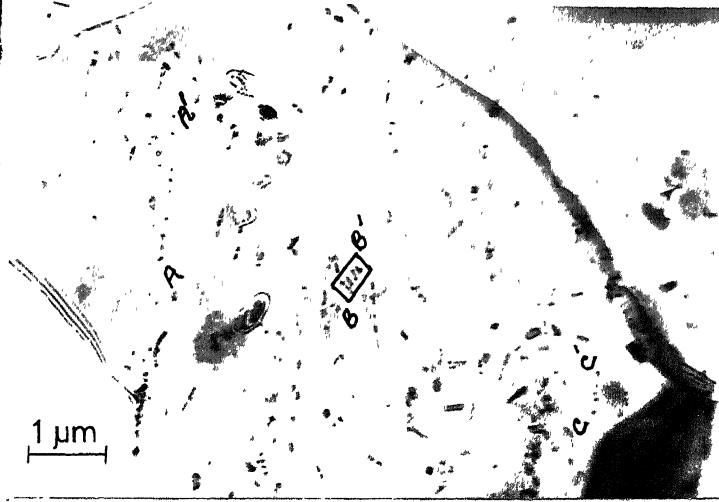
(b)

Fig.4.15 : Microstructures of precipitation-treated alloy cold worked 90% and then annealed at 300°C for 1  
 (a) recrystallized grain near insoluble  
 (b) recovered region (showing few recrystallized grains).

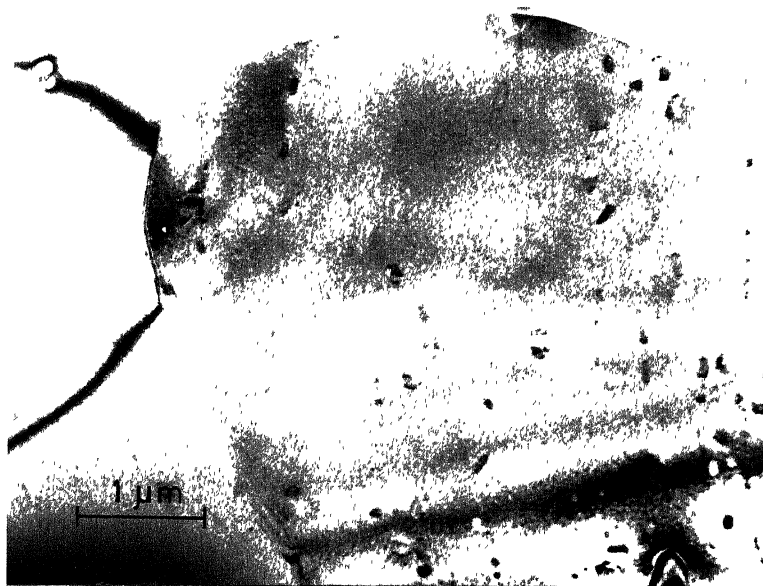




(a)



(b)



(c)

Fig.4.16 : Microstructures of precipitation-treated alloy cold worked 90% and then heated to 350°C for 1 h .  
 (a) recrystallized grains  
 (b) precipitate distribution inside recrystallized & grains and at grain boundary.  
 (c)

350°C for 1h. All the Figs.4.16(a), (b) and (c) show recrystallized grains with secondary precipitate particles remaining evenly distributed throughout the grains. The typical precipitate density in this case being  $2.5 \times 10^{19}/\text{m}^3$ . As seen from all the micrographs present in Fig. 4.16, the precipitates are very fine in nature; moreover, they remain evenly distributed throughout the strain-free grains. So, most probably these precipitate particles have come out of solution only after recrystallization was over. Otherwise, since they are below critical size required for nucleation, they would have instead hindered recrystallization. Marks AA', BB' and CC' in Fig.4.16(b) show the formation of precipitate particles at dislocations.

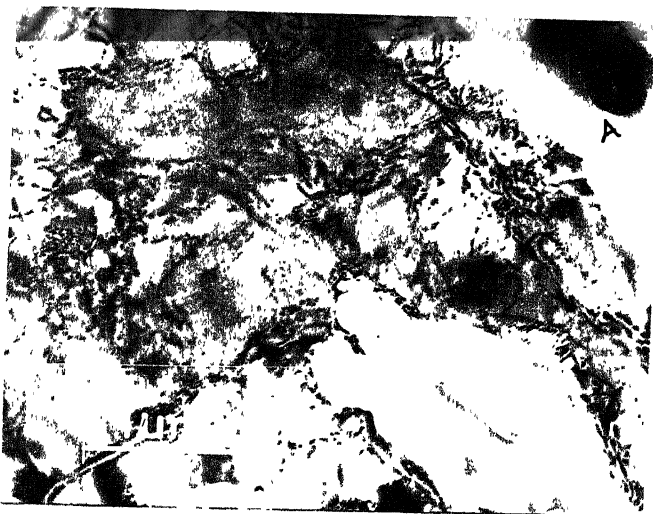
A very careful observation of all the micrographs in Fig.4.17 shows that for the P.T. (400°C), 60% cold deformed alloy, very little recrystallization has occurred on being annealed at 250°C for 1h. Fig. 4.17 (a and b) show some region where recovery is almost complete; sub-grain boundaries are clearly seen; in fact sub-boundary thinning process has already initiated inside some grains. Grain A in Fig.4.17(a) is a strain-free grain showing high angle boundary. Fig.4.17(f) represents a similar situation in the region where a cluster of particles occurs. Though the mean size of the particles in this cluster is about  $0.5 \mu\text{m}$ , still we find an almost recrystallized



(a)



(b)



(c)



(d)

Fig.4.17 : Microstructures of precipitation-treated alloy, cold worked 60% and then annealed at 250°C for 1 h .

(a) & (b) recovered regions with clear sub-boundaries: some recrystallized grains are also visible.

(c) & (d) partially recovered regions near secondary precipitates.



(e)



(f)

Fig.4.17 (e) region near insoluble  
(f) recovered region near secondary precipitates



(a)



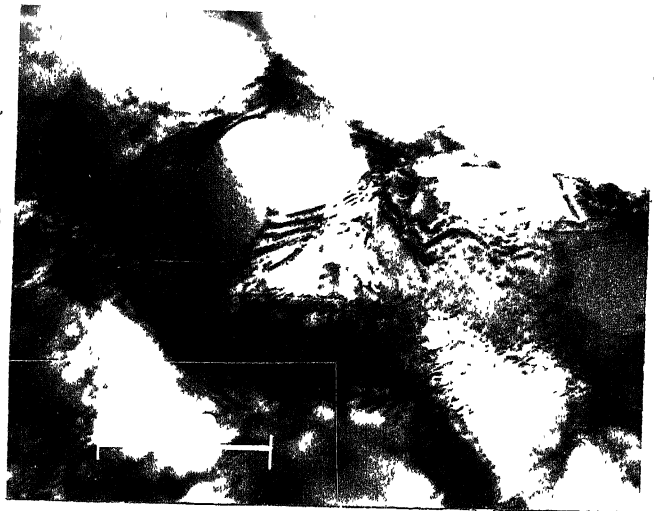
(b)

Fig.4.18 : Microstructures of precipitation-treated alloy cold worked 60% and then annealed at 300°C for 2 h .

(a) & (b) almost strain-free grains near precipitates.



(c)



(d)

Fig. 4.18 (c) & (d) : Partially recovered regions.

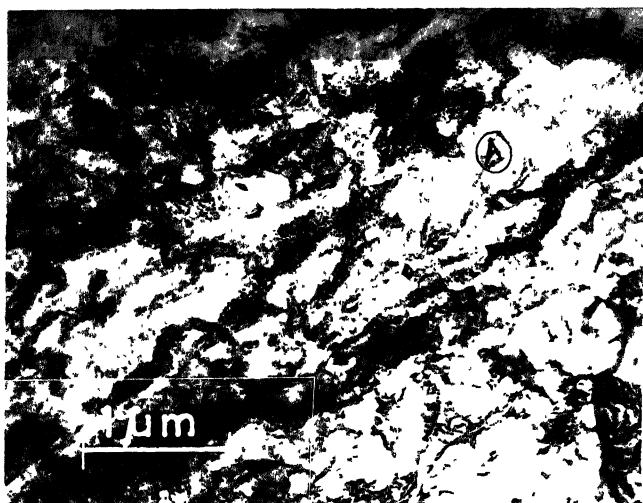


Fig.4.19(a)

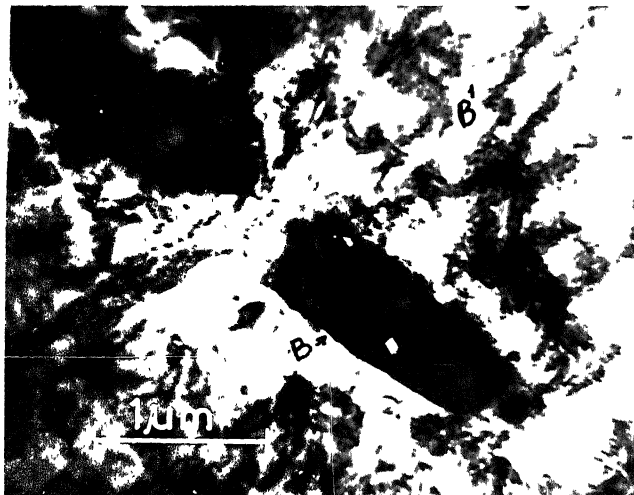


Fig.4.19(b)

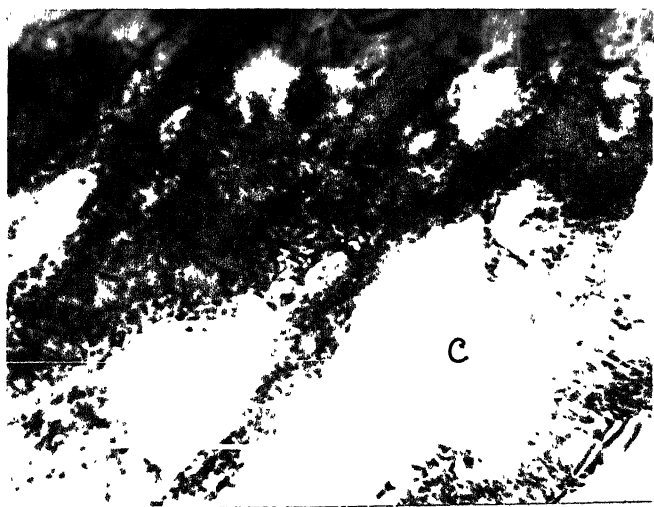


Fig.4.19(c)

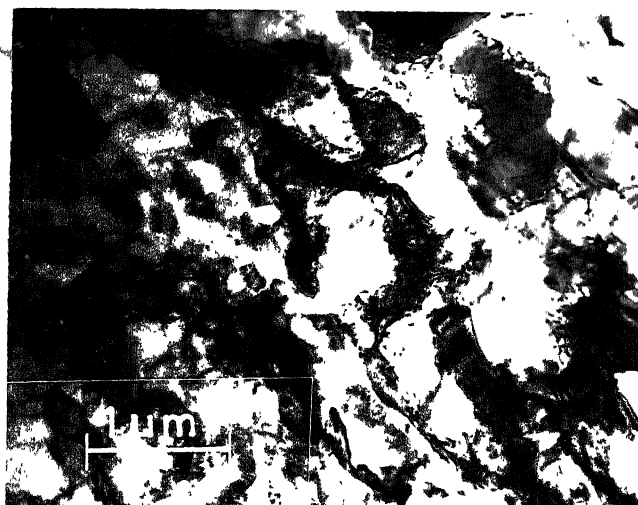


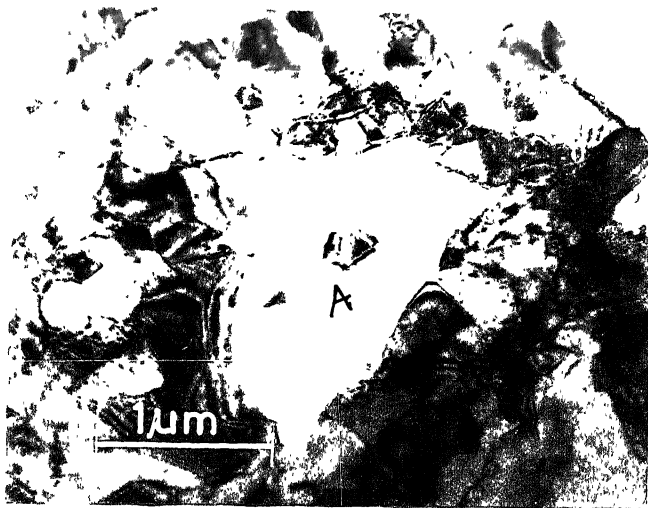
Fig.4.20(a)

Fig.4.19 : Microstructures of as-received alloy, cold worked 97%

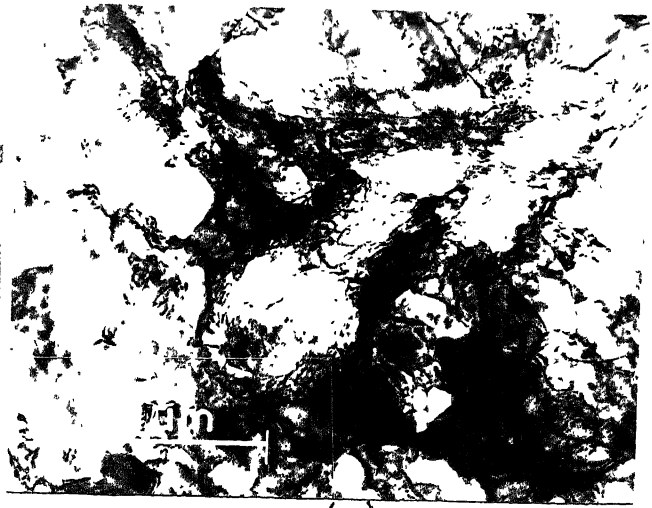
- (a) elongated cell-structure
- (b) & deformation zone around
- (c) insolubles.

Fig.4.20 : Microstructures of as-received alloy, cold worked 97% and then annealed at 250°C for 1/2 h

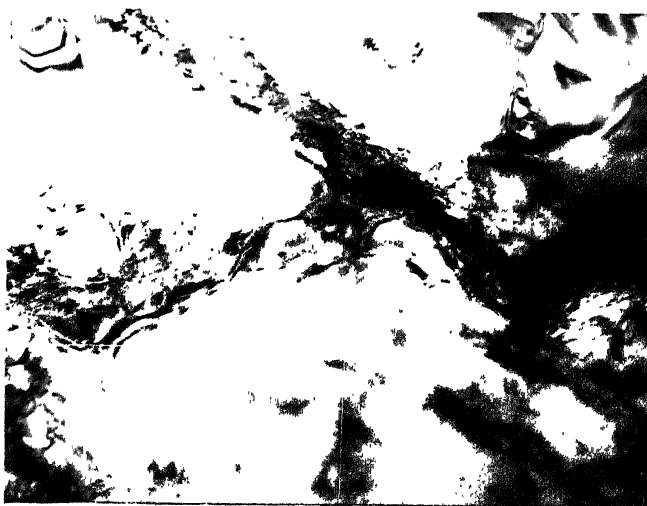
- (a) deformed-region.



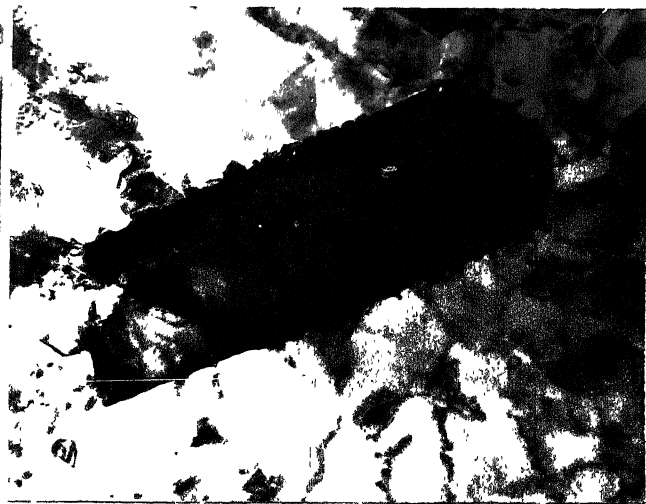
(b)



(c)



(d)



(e)

Fig.4.20 (b) & (e) : Partially recovered region around insoluble  
 (c) : Cell-structure in a region little away  
 from insolubles  
 (d) : General area.

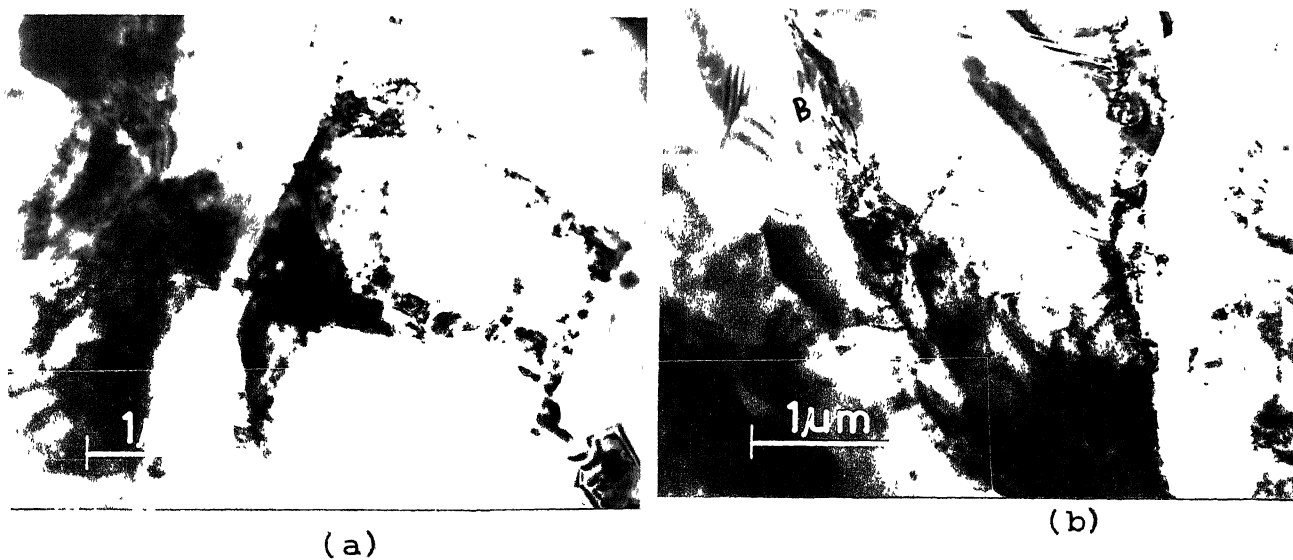


Fig.4.21 : Microstructures of as-received alloy, cold worked 97% and then annealed at 250°C for 1 h .



grain in their vicinity. Figs. 4.17(c) and (d) show partially recovered structures near secondary precipitates. ( mark 'A' and 'B' in Fig. 4.17(c) and Fig.4.17(d) respectively ) . Hence, if compared between S.T.  $\rightarrow$  60%  $\rightarrow$  250(1) and S.T.  $\rightarrow$  P.T.  $\rightarrow$  60%  $\rightarrow$  250(1), it is evident that while the former shows some recovered grains only, the latter shows almost fully recovered structure along with few recrystallized grains; moreover in the latter case, we do not find any cell structure present in the region far away from precipitates or insolubles.

Figure 4.18 shows the annealing characteristics at 300°C for 2h of a P.T. (400°, 3h) alloy cold-deformed to 60%. Fig. 4.18(a) shows particle-aided recrystallization process (Mark 'A' in Fig.4.18(a) indicates precipitate). It is evident that recrystallization process is almost complete near particles [Fig.4.18(a) and (b)] while recovery is still going on in regions away from particles [Figs.4.18(c) and (d) ] .

#### 4.4 General Discussion

The solution treated alloy contain coarse insoluble particle  $\text{Al}_{12}(\text{Fe,Mn})_3\text{Si}$ . The precipitation treated samples contain fine precipitate particles of possibly  $\text{Al}_{12}(\text{Fe,Mn})_3\text{Si}$  along with the coarse insolubles. Both these species of particles have a strong influence on the deformation structure and recrystallization characteristics of the alloy.

Aluminium has high stacking-fault energy ( $200 \text{ erg/cm}^2$ ) (41). Consequently, it has narrow stacking fault which facilitates cross slip and hence screw dislocations can move out of their original slip planes and arrange themselves in very localized regions thereby producing well defined cells. The cell walls usually have very high dislocation density. Cell structures have smaller size at higher deformation, provided other factors remain the same.

Cell formation is facilitated by the presence of additional sources of dislocation. Large widely spaced incoherent particles act as dislocation source thereby promoting cell formation. The primary insoluble particle ( $> 1 \mu\text{m}$ ) are found to facilitate cell formation in the present investigation. In case of precipitation treated 90% cold worked alloy, the cell size is found to be larger compared to that for solution treated and 90% cold worked alloy. This is because of the fact that decreasing the solute content leads to an increase in the stacking fault energy, which in turn influences the cell size.

Annealing causes annihilation of defects in a worked metal. In case of high stacking fault energy metal, such as aluminum, dislocation annihilation initiates even in the prerecrystallization stage. Now, if the dislocation movement is somehow hindered, then the kinetics of the process will be decelerated. Usually

very fine, closely spaced particles play the key role in pinning down dislocation movement, which is technically known as 'Zener drag'. However, the picture with big particles is different. The deformation zone around them are very high energy sites which can easily provide surface energy required for nucleation of strain-free grains. Once nucleated, these nuclei can easily sweep through the deformed region and in the process lowers the energy of the region. In our present investigation we have found that primary insoluble particles always aid recrystallization process.

Nes and Embury (40) studied the recrystallization behaviour of a material containing a duplex structure. They found that although the large particles still acted as nucleation sites, their performance was drastically affected by varying the surrounding particle dispersion level. Since, the fine particle dispersion try to stabilize the subgrain structure, then only those subgrain with a diameter above a critical size will be able to grow.

The elementary step in recrystallization is the movement of low or high angle boundaries. Precipitation during or before the movement of the boundary and the segregation of soluce atoms to the deformed and or to the recovered structure and to the recrystallization front are the important factors controlling recrystallization. The interaction between precipitation or segregation and

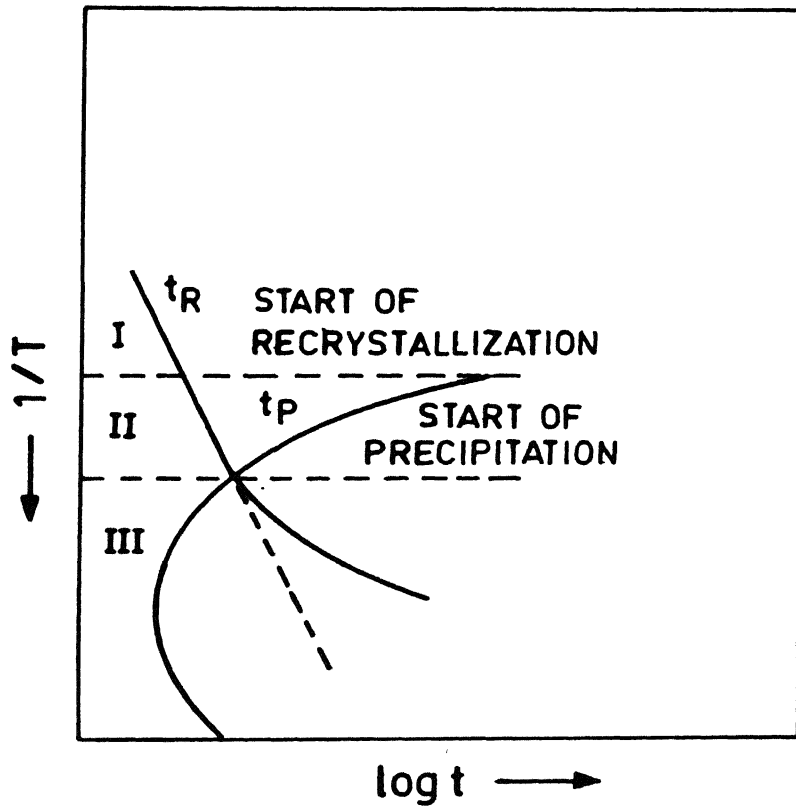


Fig. 4.22 Interaction between recrystallization and precipitation.

recrystallization can be understood by considering the time-temperature diagram shown in Fig. 4.22. At high temperature, the process of recrystallization is completed before the onset of precipitation (region I in Fig. 4.22). Moreover the recrystallization front is relatively unaffected by segregation due to high rates of diffusion of manganese atoms at these temperature. When the rates of precipitation and recrystallization are comparable (region II in Fig. 4.22), the two phenomena occur simultaneously and the mobility of the recrystallization front can be adversely affected by the precipitate particles. In region III of Fig. 4.22, precipitation precedes recrystallization and if the particle size and interparticle spacing are in the favourable range, the recrystallization process may be retarded. In case of S.T., 90% deformed alloy, precipitation is found to take place simultaneously with recrystallization at 350°C. Even then recrystallization is found to be completed. If the precipitates that are coming out on annealing are larger than the critical radius corresponding to the annealing temperature, then there will not be any Zener drag upon the migrating sub-boundary. We find in our present investigation that large ( $\approx 1.2\mu\text{m}$ ) sub-boundary particles form on annealing at 350°C for 1h while fine precipitates come out inside the grain. Probably, the fine, closely-spaced precipitates have formed only after recrystallization while sub-boundary particles <sup>have</sup> formed during recrystallization.

## CHAPTER 5

### CONCLUSIONS

On the basis of the results and discussion presented in Chapter 4, the following conclusions can be drawn:

1. The rolling texture is found to be close to the (111)  $[uvw]$  type, in general, for both solution treated as well as precipitation treated alloys.
2. Precipitates particles showed almost no effect on rolling texture.
3. For S.T. and P.T. alloy, deformed 90% and then annealed at 350°C for 1h, random texture is observed.
4. Rolling texture component was found to exist even in the samples annealed at 300°C and 350°C for both S.T. and P.T. alloys.
5. Homogenization of the alloy at 620°C for 24h does not lead to complete dissolution of manganese. Primary insoluble particles of  $Al_{12}(Fe, Mn)_3Si$  are present after this treatment.
6. Cold rolled samples of the alloys show well-developed cell structure; the mean cell size is 0.3  $\mu m$  for the solution-treated alloy deformed to 90%. However, the cell size for the precipitation

treated alloy deformed to 90% is much large ( $\approx 1.15 \mu\text{m}$ ).

7. Cell structures are observed in solution treated alloy, cold-deformed 60% and then annealed at  $250^\circ\text{C}$  for 1h, in regions away from insolubles; however, for the precipitation treated alloy, given the same subsequent treatments, there is strong evidence of recovery.
8. The process of recrystallization is complete for both S.T. and P.T. alloys, deformed to 90%, at  $350^\circ\text{C}$ .
9. In general, the size of precipitate is larger in the S.T. alloy, compared to the cold-worked alloy.
10. Recrystallization nuclei were found to come out first, in the vicinity of large particle.

## REFERENCES

1. Mn in Al-alloys, L.F. Mondolfo, page 3.
2. Mn in Al-alloys, L.F. Mondolfo, page 3.
3. T. Onishi, Y. Naketani, J. Jap. Inst. Light Metals, 1975, 25, 253.
4. Mn in Al-alloys, L.F. Mondolfo, page 10.
5. Mn in Al-alloys, L.F. Mondolfo, page 27.
6. Mn in Al-alloys, L.F. Mondolfo, page 27.
7. Mn in Al-alloys, L.F. Mondolfo, page 27.
8. E. Dartyge and Coll., Acta Met., 1972, 20, 233.
9. Mn in Al-alloys, L.F. Mondolfo, page 29.
10. Mn in Al-alloys, L.F. Mondolfo, page 29.
11. D.B. Goel and Coll., Aluminium, 1974, 50, 511, 641.
12. Mn in Al-alloys, L.F. Mondolfo, page 37.
13. Mn in Al-alloys, L.F. Mondolfo, page 38.
14. Mn in Al-alloys, L.F. Mondolfo, page 42.
15. Mn in Al-alloys, L.F. Mondolfo, page 46.
16. R.D. Heidenreich., J. Appl. Phys., 20 (1949) 993.
17. S. Weissmann, T. Imura and N. H. Sakawa, Recovery and Recrystallization in Metals, ed. L. Himmel, Interscience, N.Y., 1963, 246.
18. P.B. Hirsch, Internal Stresses and Fatigue in Metals, G.M. Rassweiler and G.L. Grube, Elsevier, Amsterdam, 1958, 139.
19. P. Gay and A. Kelly, Acta Crystallogr., 6 (1953) 172 and 185.
20. G. Thomas, Phil. Mag., 4 (1959) 1213.
21. R. Vandervoort and J. Washburn, Phil. Mag., 5 (1960) 24.



22. P.R. Swann, *Electron Microscopy and Strength of Crystals*, ed. G. Thomas and J. Washburn, Interscience, NY, 1963, 131.
23. A.R. Jones and N. Hansen, 'Recovery Changes Leading to Nucleation of Recrystallization.
24. F.J. Humphreys, 'The Nucleation of Recrystallization at Second Phase Particles in Deformed Aluminum', *Acta Met.* 25 (1977), 1323-1344.
25. P. Herbst and J. Huber, 'Orientation of Recrystallization Nuclei in a Deformed AlMgSi 1-alloy', 5th Int. Conf. Textures of Materials I, Eds. G. Gottstein and K. Lucke, Springer, Berlin (1978), 453-464.
26. R. Sandstrom, 'Formation and Growth of Recrystallization Nuclei Around Particles, *Z. Metallkunde*, 1980.
27. F.J. Humphreys, 'Models and Mechanisms proposed to explain the Strengthening of Metals by Oxide Particles, In: Proc. 22nd Colloque de Metallurgie de Saclay 1979 *Ann. Chim. Fr.* (1980), 5, 25-48.
28. F. Gatto, G. Camona, M. Conserva and P. Fiorini, *Mater. Sci. Engg.*, 3 (1968/69) 56.
29. D.B. Goel, P. Ferrer and H. Warlimont, *Aluminum*, 50 (1974), 641.
30. D.B. Goel, P. Ferrer and H. Warlimont, *Aluminum*, 50 (1974) 511.
31. Sandstrom, R. (1977a), 'Subgrain Growth Occurring by Boundary Imagination', *Acta Met.* 25, 905-911.
32. Sandstrom, R. (1977b), 'On Recovery Dislocations in Subgrain and Subgrain Coalescence, *Acta. Met.* 25, 897-904.
33. Barrett S.C., *Structure of Metals*, p. 492.
34. Chan, H.M. and Humphreys, F.J., 'Effect of Particle Stimulated Nucleation on Orientation of Recrystallized Grains', *Metal. Sci.* 18, Nov. 84, 527.
35. Bleck and Bunge, *Acta Metall.*, 1981, 29, 1401.
36. Dillamore, I.L., Smith, C.J.E., W.B. (1972), *Transition Band and Recrystallization in Metals*, 329A, 405-420.

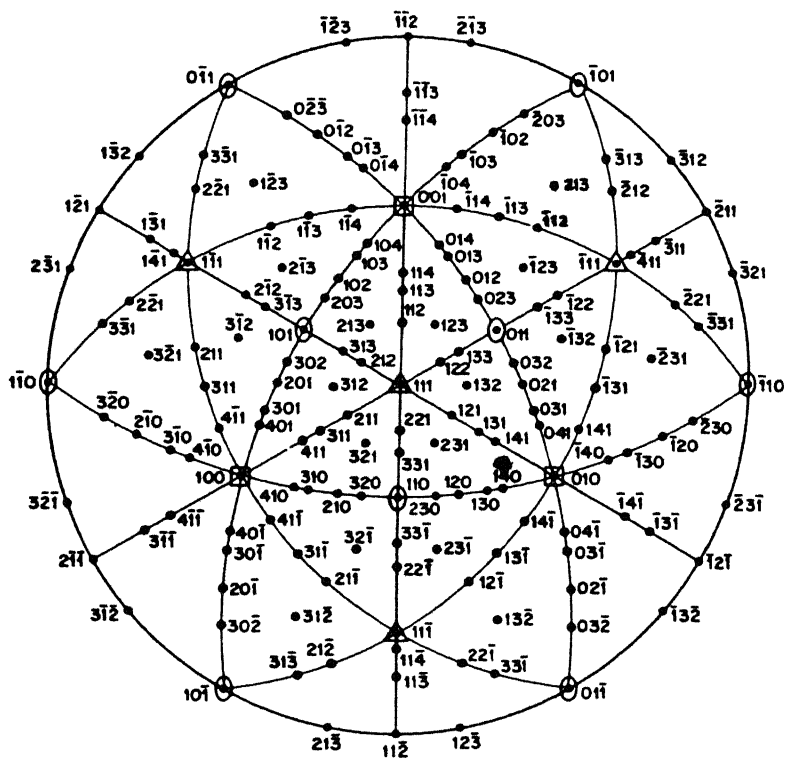
37. Faivre, P. and Doherty, R.D. (1979), Nucleation of Recrystallization in Compressed Aluminium-studies by Electron Microscopy and Kikuchi Diffraction, J. Mat. Sci., 14, 897-919.
38. Bay, B. and Hansen, N. (1979), Initial Stages of Recrystallization in Aluminium of Commercial Purity, Met. Trans. A, 10A, 279-288.
39. Gokhale, A.M., Estimation of Average-size of Convex Particles, Met. Trans. A.
40. E. Nes and J.D. Embury, Z. Metallk, 66, 589 (1975).
41. Cotterill, P. and Mould, P.R., 'Recrystallization Studies and Grain Growth in Metals, p. 19.

Table I-1  $\text{Al}_{12}(\text{FeMn})_3\text{Si}(\text{BCC})$ 

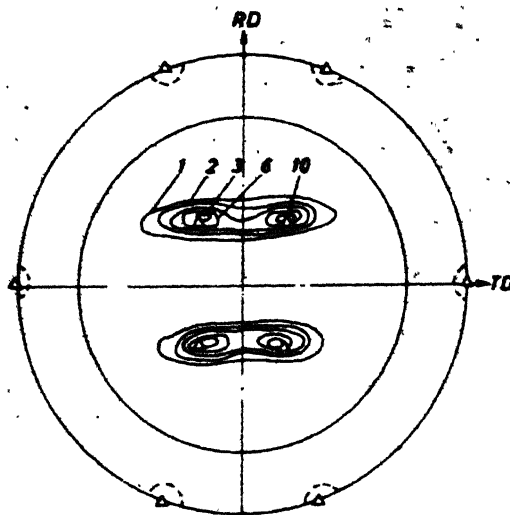
$$a = 12.65 \text{ \AA}$$

hkl	d(Å)	hkl	d(Å)
110	8.940	116	2.05
002	6.32	055	1.77
112	5.16	345	1.77
022	4.47	017	1.77
103	4.00	026	2.00
222	3.65	145	1.95
132	3.38	226	1.91
004	3.16	136	1.87
114	2.98	444	1.83
033	2.98	046	1.75
042	2.82	255	1.72
233	2.69	336	1.72
224	2.58	127	1.72
015	2.48	246	1.69
134	2.48	037	1.66
251	2.30	156	1.61
044	2.23	237	1.61
343	2.16	008	1.58
305	2.16	118	1.56
244	2.10	147	1.56
006	2.10	455	1.55
325	2.05	028	1.53

APPENDIX - II



(111) Standard projection of cubic crystal.



$\Delta$  (110)  $[\bar{1}12]$

A-III. (111) Pole Figure showing (110)  $\bar{1}12$  Orientation

A 92031

Th  
669.95722 Date Slip 92031  
B469 Y

This book is to be returned on the  
date last stamped.


ME-1986-M-BHA-REC